MNRAS 000, 1–19 (2019) Preprint 17 March 2024 Compiled using MNRAS LATEX style file v3.0

Extensions to models of the galaxy-halo connection

Boryana Hadzhiyska,[1]★ Sownak Bose,[1] Daniel Eisenstein,[1] Lars Hernquist[1]
[1]*Harvard-Smithsonian Center for Astrophysics, 60 Garden St., Cambridge, MA 02138, USA*

Accepted XXX. Received YYY; in original form ZZZ

ABSTRACT

We explore two widely used empirical models for the galaxy-halo connection, subhalo abundance matching (SHAM) and the halo occupation distribution (HOD) and compare their predictions with the state-of-the-art hydrodynamical simulation IllustrisTNG (TNG) for a range of statistics that quantify the galaxy distribution at $n_{\rm gal} \approx 1.3 \times 10^{-3}\,[{\rm Mpc}/h]^{-3}$. We observe that in their most straightforward implementations, both models fail to reproduce the two-point clustering measured in TNG. We find that SHAM models constructed using the relaxation velocity, $V_{\rm relax}$, and the peak velocity, $V_{\rm peak}$, perform best, and match the clustering reasonably well, although neither model captures adequately the one-halo clustering. Splitting the total sample into sub-populations, we discover that SHAM overpredicts the clustering of high-mass, blue, star-forming, and late-forming galaxies and uderpredicts that of low-mass, red, quiescent, and early-forming galaxies. We also study various baryonic effects, finding that subhalos in the dark-mater-only simulation have consistently higher values of their SHAM-proxy properties than their full-physics counterparts. We then consider a two-dimensional implementation of the HOD model augmented with a secondary parameter (environment, velocity anisotropy, $\sigma^2 R_{\rm halfmass}$, and total potential) and tuned so as to match the two-point clustering of the IllustrisTNG galaxies on large scales. We analyze these galaxy populations adopting alternative statistical tools such as galaxy-galaxy lensing, void-galaxy cross-correlations and cumulants of the smoothed density field, finding that the hydrodynamical galaxy distribution disfavors $\sigma^2 R_{\rm halfmass}$ and the total potential as secondary parameters, while the environment and velocity anisotropy samples are consistent with full-physics across all statistical probes examined. Our results demonstrate the power of examining multiple statistics that characterize the galaxy field, which enables us to determine a hierarchy in the efficacy of secondary parameters for augmenting the galaxy-halo connection.

Key words: cosmology: large-scale structure of Universe – galaxies: haloes – methods: numerical – cosmology: theory

1 INTRODUCTION

The study of galaxy clustering provides a wonderful opportunity to learn about galaxy formation and evolution as well as the fundamental laws governing our cosmological model. Small-scale clustering offers information regarding the relationship between galaxies and their dark matter (DM) halo hosts and also stellar population properties, whereas large-scale clustering of galaxies yields insight into many of the unresolved mysteries of our Universe such as the nature of dark matter and dark energy and its cosmological makeup and early history (Peebles 1980). Computing correlation function statistics of different physical quantities at different scales allows for the breaking of multiple degeneracies among astrophysical parameters and thus can yield tighter constraints on those and, eventually, the cosmological parameters themselves.

Extracting information from galaxy clustering, however, relies on the accuracy of predictions from galaxy formation models and our cosmological theories. On small scales, this task is challenging because one enters the non-linear regime, where analytical solutions are not available, and stochastic processes such as mergers, tidal stripping, star formation, and non-linear gravitational collapse take place. These processes are best mimicked and studied in numerical simulations of which there are two types (see Kuhlen et al. 2012, for a review). The first kind implements jointly the evolution of the DM and baryon fluid together with recipes for unresolved astrophysical processes such as feedback from super-

★ E-mail: boryana.hadzhiyska@cfa.harvard.edu

novae and star formation. These so-called hydrodynamical simulations yield a direct prediction for the distribution and properties of galaxies, but the computational expense for simulating sufficiently large volumes (i.e. at volumes comparable to future galaxy redshift surveys) at an adequate resolution is great (Vogelsberger et al. 2014; Schaye et al. 2015; Lee et al. 2020; Vogelsberger et al. 2020). The current box size of these simulations is on the order of only a few hundred Mpc/h.

On the other hand, simulating gravitation-only interactions is much more inexpensive from a numerical resource point of view. To correctly mimic the statistics and systematics of observational surveys, it is necessary to model galaxy clustering in simulations with volumes on the order of 1 Gpc$^3/h^3$ (Angulo et al. 2008), which are eminently feasible in these DM-only or N-body simulations. The downside is that one needs to resort to "painting" galaxies *a posteriori*, after the simulation has been completed. This approach is supported by leading theories of galaxy formation in which the locations of galaxies are predominantly determined by the properties of the DM halos they reside in (see Vogelsberger et al. 2020, for a review). There are many recipes one can adopt for populating DM halos with galaxies, but unfortunately there is a lot of uncertainty surrounding these choices, as the relationship between halos and galaxies is not straightforward (see Wechsler & Tinker 2018, for a review).

The galaxy-halo relation is at the crux of many of the standard techniques for "painting" galaxies on top of halos, including one of the most widely used and computationally inexpensive empirical (or phenomenological) models known as the halo occupation distribution (HOD) model. In its simplest manifestation, the HOD framework describes the number of galaxies residing in a host halo as a function of halo mass (Peacock & Smith 2000; Seljak 2000; Scoccimarro et al. 2001; Berlind & Weinberg 2002), remaining agnostic about any other halo property. It rests on the long-standing and widely accepted theoretical prediction that halo mass is the attribute that most strongly influences the halo abundance and halo clustering as well as the properties of the galaxies in it (White & Rees 1978; Blumenthal et al. 1984). The HOD model is currently a popular choice for building mock galaxy catalogs and interpreting observations of the correlation function of galaxies, leading to constraints on the typical halo masses of observed galaxies and on the values of cosmological parameters (Zhai et al. 2019).

Another empirical method for populating collisionless N-body simulations is called the subhalo abundance matching (SHAM) method (e.g. Vale & Ostriker 2007; Conroy et al. 2006). In its original implementation, SHAM assumes an injective and monotonic relation between galaxies and self-bound DM structures (subhalos) based on a pair of specified parameters. Typically one associates the most massive galaxies, in terms of their stellar mass, with the most massive DM subhalos, where one often uses velocity-related subhalo properties as mass proxies such as the maximum circular velocity. To introduce more realism, recent implementations have also introduced stochasticity into that relation, (e.g. Behroozi et al. 2010; Reddick et al. 2014). The thus obtained galaxies are placed at the centers of the subhalos and given the same velocity as their corresponding subhalos. SHAM in its original form, thus makes predictions for the clustering of galaxies, but not for any physical galaxy properties such as stellar mass, star formation rate, metallicity, etc. SHAM-derived galaxy catalogs have been shown to reproduce the observed galaxy clustering over a broad redshift range across different datasets, (e.g. Nuza et al. 2013; Reddick et al. 2014; Simha & Cole 2013). On the other hand, comparisons with hydrodynamical simulations have yielded less conclusive results, depending on the choice of SHAM subhalo proxy, redshift of interest and choice of galaxy density (e.g. Simha et al. 2012; Chaves-Montero et al. 2016; Contreras et al. 2020). It is important to consider that any such comparison is strongly dependent on the galaxy formation and evolution models adopted in the hydro simulations. The 'precision cosmology' goals of future galaxy surveys will place even more stringent demands regarding the accuracy of the population models employed.

One of the main limitations to improving the accuracy of the galaxy clustering measurements and systematics thereof is the way in which these models handle "galaxy assembly bias", which is a manifestation of the large-scale discrepancy between the DM distribution and that of galaxies. Assembly bias refers to details of the galaxy-halo connection related to halo assembly history beyond just present-day halo mass (Croton et al. 2007) such as halo formation time, environment, concentration, triaxiality, spin, and velocity dispersion. Galaxy assembly bias results from two effects: halo assembly bias and occupation variation. The former manifests itself as a difference in the halo clustering among halos of the same mass that differ in some secondary property (e.g. formation time, concentration, spin, Gao et al. 2005), while the latter comes from the dependence of the galaxy population on properties of the halo host other than its mass (Zehavi et al. 2018; Artale et al. 2018).

The standard (mass-only) implementation of the HOD does not consider halo properties apart from its mass and hence does not incorporate galaxy assembly bias effects. On the other hand, the subhalo abundance matching techniques have an intrinsic dependence on the halo assembly history – recently-formed halos tend to have richer substructure, i.e. more subhalos. However, the baseline SHAM model disregards baryonic effects on processes internal to halos, such as tidal stripping and subhalo disruption, which may affect our ability to link subhalos in N-body simulations to those in hydro simulations. The most straightforward versions of both models also fail to implement a dependence on environmental properties, which have recently been supported through a growing body of evidence (e.g. Ramakrishnan et al. 2019; Mansfield & Kravtsov 2019; Hadzhiyska et al. 2020).

There have been several attempts to incorporate assembly bias into the HOD framework (Paranjape et al. 2015; Hearin et al. 2016; Yuan et al. 2018; Wang et al. 2019; Zentner et al. 2019; Vakili & Hahn 2019), most of which have used halo concentration (or closely related quantities as proxies) as the main halo property. This parameter has been shown, however, to be insufficient in reproducing the full galaxy assembly bias signal (Croton et al. 2007; Hadzhiyska et al. 2020; Xu & Zheng 2020). Other parameters such as environment have not been explored as thoroughly in the literature (McEwen & Weinberg 2016; Xu & Zheng 2020). There has also been a small number of works attempting to model assembly bias in SHAM, e.g. Lehmann et al. (2017); Contreras et al. (2020).

Understanding the effect of assembly bias is extremely

important since, if modeled incorrectly, it can lead to substantial biases in the inferred constraints on cosmological and galaxy formation properties. One way to check whether the modeling for future surveys is done at the required levels of precision is by testing extensions to these empirical models against hydrodynamical simulations. In this paper, we explore the agreement (or not, as the case may be) between the state-of-the-art hydrodynamical simulation IllustrisTNG (TNG) and the two most widely used empirical models for populating galaxies, SHAM and HOD. We first study which SHAM parameter choices exhibit the least amount of discrepancy compared with TNG, delving into details of the galaxy sub-populations captured best by the model (e.g. red vs. blue galaxies, satellites vs. centrals, etc.) and commenting on differences between the subhalo populations in the DM-only and full-physics simulation runs. Next we consider a two-dimensional implementation of the HOD model (2D-HOD), first introduced in Hadzhiyska et al. (2020), tuned so as to reconcile the differences between the large-scale correlation function of the model and the hydro simulation. Finally, we compare other statistical properties of the two samples such as galaxy-galaxy lensing, void functions, and cumulants of the smoothed density field, commenting on the most appropriate secondary parameter choices.

2 METHODS

Here we describe the hydrodynamical simulation employed in this study, IllustrisTNG, and two standard empirical galaxy population models, HOD and SHAM, which are commonly used to populate N-body simulations and are relatively straightforward to implement and computationally inexpensive to run. We test the assumptions of these models on the DM-only IllustrisTNG simulation and compare them with the corresponding full-physics galaxy sample. Combining the two datasets allows us to draw direct statistical comparisons between the "truth" (defined by the full-physics run) and the two population models.

2.1 IllustrisTNG

In this paper, we consider the hydrodynamical simulation IllustrisTNG (TNG) (Pillepich et al. 2018; Marinacci et al. 2018; Naiman et al. 2018; Springel et al. 2018; Nelson et al. 2019a; Nelson et al. 2018; Pillepich et al. 2019; Nelson et al. 2019b). TNG is a suite of magneto-hydrodynamic cosmological simulations, which were carried out using the AREPO code (Springel 2010) with cosmological parameters consistent with the *Planck 2015* analysis (Planck Collaboration et al. 2016). These simulations feature a series of improvements compared with their predecessor, Illustris, such as improved kinetic AGN feedback and galactic wind models, as well as the inclusion of magnetic fields.

In particular, we will use Illustris-TNG300-1 (TNG300 thereafter), the largest high-resolution hydrodynamical simulation from the suite. The size of its periodic box is 205 Mpc/h with 2500^3 DM particles and 2500^3 gas cells, implying a DM particle mass of $3.98 \times 10^7\ M_\odot/h$ and baryonic mass of $7.44 \times 10^6\ M_\odot/h$. We also employ its DM-only counterpart, TNG300-Dark, which was evolved with the same initial conditions and the same number of dark matter particles (2500^3), each with particle mass of $4.73 \times 10^7\ M_\odot/h$. This gives us an opportunity to make a halo-by-halo assignment of galaxies by cross-matching the full-physics and DM-only simulations. The halos (groups) in TNG are found with a standard friends-of-friends (FoF) algorithm with linking length $b = 0.2$ run on the dark matter particles, while the subhalos are identified using the SUBFIND algorithm (Springel et al. 2001), which detects substructure within the groups and defines locally overdense, self-bound particle groups. We analyze the simulations at the final redshift, $z = 0$.

2.2 SHAM

We first consider the empirical galaxy population model called "subhalo abundance matching" or SHAM. In its simplest form, it assumes a perfect match between stellar mass (or luminosity) as obtained from a hydrodynamical simulation or galaxy survey and a subhalo property output by the corresponding N-body run. The latter property can simply be the total DM mass of the subhalo, but recently SHAM models have preferentially been using velocity-related parameters, as they are deemed more resilient to tidal stripping and other disruptive processes resulting after the initial subhalo infall (e.g. Guo et al. 2016). A growing body of evidence has also suggested that populating subhalos based on their early-history properties (e.g. velocity at time of infall or peak circular velocity) also leads to a better agreement with observed galaxy clustering (e.g. Chaves-Montero et al. 2016). Finally, other SHAM implementations also include scatter in the mapping between hydrodynamical and DM-only objects to mimic what is empirically seen in observations (Contreras et al. 2020).

2.3 HOD

The main assumption of the standard HOD model is that the number of galaxies belonging to a halo is determined probabilistically by the mass of that halo. Typically, the HOD model has a functional form with several free parameters which describe the central and satellite mean occupation functions as a function of mass, $N_{\rm cen}(M_{\rm h})$ and $N_{\rm sat}(M_{\rm h})$, respectively. For each halo, the number of galaxies is then sampled from these distributions. A widely used example of this functional form was introduced in Zheng et al. (2005)

$$\langle N_{\rm cen}(M_{\rm h})\rangle = \frac{1}{2}\left[1 + {\rm erf}\left(\frac{\log M_{\rm h} - \log M_{\rm min}}{\sigma_{\log M}}\right)\right] \quad (1)$$

$$\langle N_{\rm sat}(M_{\rm h})\rangle = \left(\frac{M_{\rm h} - M_{\rm cut}}{M_1}\right)^{\alpha}, \quad (2)$$

where $M_{\rm min}$ is the characteristic minimum mass of halos that host central galaxies, $\sigma_{\log M}$ is the width of this transition, $M_{\rm cut}$ is the characteristic cut-off scale for hosting satellites, M_1 is a normalization factor, and α is the power-law slope. As halo mass proxy, $M_{\rm h}$, the definition we adopt here is $M_{\rm 200m}$, which is the total mass within a sphere with mean density 200 times the mean density of the Universe.

In Fig. 1, we show the HOD derived from TNG300 at $n_{\rm gal} \approx 1.3 \times 10^{-3}\ [{\rm Mpc}/h]^{-3}$, a galaxy number density close

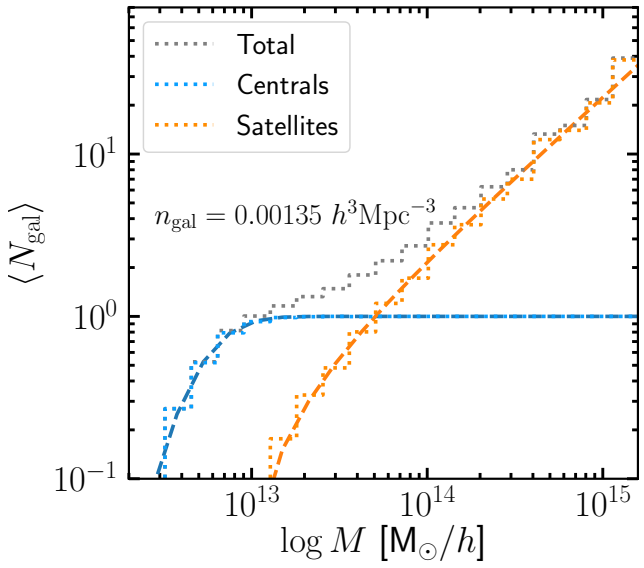

Figure 1. Histogram of the mean number of galaxies per halo as a function of halo mass (halo occupation distribution) in TNG300. Here, we use $M_{\rm 200m}$ as the halo mass definition and break the galaxy sample into two populations – centrals and satellites. We also show fits (*dashed line*) to these populations assuming the 5-parameter HOD model described in the text (Zheng et al. 2005).

to the anticipated one in future galaxy surveys. The figure demonstrates that Eqs. 1 and 2 capture the overall shape of the HOD from our simulations very well. The corresponding best-fit values for the 5 free parameters of this model are: $\log M_{\rm min} = 12.712$, $\sigma_{\log M} = 0.287$, $\log M_{\rm cut} = 12.95$, $\log M_1 = 13.62$ and $\alpha = 0.98$.

2.3.1 "Basic" HOD

Throughout this paper, we will be referring back to the galaxy sample derived via a mass-only prescription of the HOD model, which we dub "basic" HOD. This was introduced in Hadzhiyska et al. (2020), where it was found that the "basic" HOD model leads to a discrepancy of $\sim 15\%$ in the two-point clustering compared with the hydrodynamical simulation (see also Croton et al. 2007; Beltz-Mohrmann et al. 2019). We outline the procedure below:

1. Bijectively match as many of the halos across the dark-matter-only (DMO) and full-physics (FP) TNG300-1 simulations (close to 99% in the mass range of interest). Keep track of how many galaxies the corresponding DM-only halos would receive from this match.
2. Split the halos into mass bins such that the fractional change within each is $\frac{M_{\rm max}-M_{\rm min}}{M_{\rm avg}} \lesssim 5\%$.
3. Order the DM-only halos by mass and, within each mass bin, reassign the number of galaxies by randomly shuffling them. We exclude the 100 most massive halos because the halo mass function contains very few examples of such high-mass systems.
4. The galaxies within a given halo are assigned to the subhalos in descending order of their $V_{\rm peak}$ velocity (peak magnitude of the circular velocity attained by the subhalo at any point in its evolution). The $V_{\rm peak}$ assignment has been shown to provide a good match to the radial distribution of satellites (see Bose et al. 2019).

Fig. 1 remains unchanged after performing a shuffling of the occupation numbers in 5% mass bins following the recipe described above, so any deviations from the full-physics galaxy samples are suggestive of violations of some of the HOD model assumptions.

2.3.2 "Fitted" 2D-HOD

As shown in Hadzhiyska et al. (2020), the parameters that are most influential in shifting the large-scale clustering in the direction of the hydro simulation result are the local environment parameter, $f_{\rm env}$, the velocity anisotropy, β, and the dynamical mass proxy, $\sigma^2 R_{\rm halfmass}$, which we will review in Section 4.1. We do this assuming a perfect association of ranks between the halo occupation and the second parameter (e.g. the halo with the largest value of $f_{\rm env}$ gets assigned the largest number of galaxies in each 5% mass bin). However, in order to recover the clustering of galaxies in TNG300, we need to introduce a scatter into this relation, effectively obtaining a two-dimensional HOD (2D-HOD) prescription.

Here we introduce a reordering procedure which, like the "basic" HOD model described in Section 2.3.1, preserves the occupation numbers of the full-physics halos, but matches the clustering of the full-physics galaxies on large-scales (see also Hadzhiyska et al. 2020). This is accomplished by introducing scatter between the halo occupation number within each mass bin and a halo parameter of interest, $p_{\rm match}$.

For each 5%-mass bin, which contains $N_{\rm h}$ halos,

1. We choose a correlation parameter, r, between 0 and 1 and draw $N_{\rm h}$ pairs of (x, y) values from a joint Gaussian distribution with mean $[0, 0]$ and covariance matrix $[[1, r], [r, 1]]$.
2. We convert the array of $\{(x, y)\}$ pairs into an array of pairs of integers by assigning an integer value to each entry of both $\{x\}$ and $\{y\}$, $\{(x, y)\} \rightarrow \{(i, j)\}$, where i and j are integers between 1 and $N_{\rm h}$ determined by the rank in descending order of each of the elements in the original $\{x\}$ and $\{y\}$ arrays, respectively.
3. We form two new arrays: one containing the occupation number of the halos in that mass bin, $\{N_{\rm gal}\}$, and one containing the values of the halo property of interest, $\{p_{\rm match}\}$.
4. We then directly associate the drawn array of $\{(i, j)\}$ pairs with the two halo property arrays, so that for a given pair $(\tilde{i}, \tilde{j})$ the halo with $\tilde{j}^{\rm th}$ highest parameter value $p_{\rm match}$ receives the $\tilde{i}^{\rm th}$ highest halo occupation number in that bin.

To obtain the amount of correlation, r, between the number of galaxies per halo and the halo property of choice, $p_{\rm match}$, we minimize the χ^2-value of the auto-correlation function, $\xi(r)$, on large scales between the 2D-HOD derived sample and the hydrodynamical galaxy sample

$$\chi^2 = \sum_i \frac{(\xi_{i,\ \rm TNG300} - \xi_{i,\ \rm 2D-HOD})^2}{\sigma^2_{i,\ \xi}}, \tag{3}$$

where i varies between 1 and the number of radial bins and $\sigma_{i,\ \xi}$ is the jackknife error of the two-point correlation function of the full-physics sample in the $i^{\rm th}$ radial bin. We tune

the clustering for 10 radial bins in the range of 1 Mpc/h to 20 Mpc/h.

2.4 Jackknife errors

To obtain a measure of the errors associated with our various statistical tools (correlation functions, void size histograms, density field moments), we split the volume of the simulation into $3^3 = 27$ equal parts and define 27 subsamples by excluding in each a different cube of side (205/3) Mpc/$h \approx 68$ Mpc/h from the total volume. We then estimate the statistics of interest for the galaxy samples in each of the 27 subsamples and compute their mean and standard deviation.

As an example, let us consider the estimation of errorbars in the galaxy clustering. We first compute the correlation functions in each of the 27 subsamples using the Landy-Szalay estimator (Landy & Szalay 1993)

$$\xi_{\rm LS}(r) = \frac{DD(r)}{RR(r)} - 1, \tag{4}$$

assuming periodic boundary conditions. To obtain the correlation function and corresponding errors for the full box, we calculate the mean and jackknife errors of the correlation functions (and their ratios) adopting the standard equations

$$\bar{\xi}(r) = \frac{1}{n}\sum_{i=1}^{n}\xi_i(r) \tag{5}$$

$$\mathrm{Var}[\xi(r)] = \frac{n-1}{n}\sum_{i=1}^{n}(\xi_i(r) - \bar{\xi}(r))^2, \tag{6}$$

where $n = 27$ and $\xi_i(r)$ is the correlation function value at distance r for subsample i (i.e. excluding the galaxies residing within volume element i in the correlation function computation).

3 SHAM MODELING

The analysis performed in this section uses the 12000 most massive subhalos (defined by their stellar mass) in the TNG300 simulation (resulting in a number density of $n_{\rm gal} \approx 1.3 \times 10^{-3}$ $[\mathrm{Mpc}/h]^{-3}$). In this way, we attempt to limit our study to well-resolved galaxies and obtain number densities closer to the currently observed ones in galaxy surveys (e.g. DESI, *Euclid*).

3.1 Abundance-matching the full-physics and DM-only simulations

We implement a SHAM prescription, where we rank-order the subhalos in the DM-only run based on one of 8 proxy parameters and those in the full-physics run based on their stellar mass. We do not input any scatter into the relation, as we are interested in seeing whether the assumption of perfect correlation between the SHAM property and stellar mass would yield good agreement with the hydro simulation. Furthermore, we want to compare overall trends of the model using different parameters, so not adding stochasticity makes this process easier. The SHAM parameters we use as proxies for subhalo stellar mass are

- $V_{\rm relax}$: the maximum circular velocity reached by the subhalo during the periods of its history in which it satisfies a relaxation criterion. The relaxation criterion, the definition of which can be found in Ludlow et al. (2012); Chaves-Montero et al. (2016), is motivated by the assumption that a subhalo needs about one crossing time to return to equilibrium after a major merger. Following Chaves-Montero et al. (2016), we approximate the crossing time at a given redshift as $t_{\rm cross} = 2\ R_{\rm 200m}/V_{\rm 200m} \approx 0.2/H(z)$ and compare it with the lookback time to the moment where the subhalo reaches 3/4 of its mass at the considered redshift (the particular choice of 3/4 has been shown not to make a difference to the final result). Finally, we conjoin all times where this criterion is satisfied and find the highest circular velocity of the subhalo across these epochs.
- $V_{\rm peak}$: the maximum circular velocity reached by the subhalo throughout its history.
- $V_{\rm max}$: the maximum circular velocity of the subhalo at the final time (i.e. $z = 0$).
- $V_{\rm infall}$: the maximum circular velocity of the subhalo at the time when it falls into a larger halo and ceases to be recognized as a central.
- $M_{\rm peak}$: total mass of the bound particles in a subhalo at the time when it achieves its peak mass.
- $M_{\rm infall}$: the total mass of bound particles in a subhalo at the time when the subhalo infalls into a (larger) halo and becomes a satellite of that halo. For central subhalos, this quantity is equivalent to $M_{\rm SUBFIND}$,
- $M_{\rm SUBFIND}$: the total mass of bound particles in a subhalo defined by the SUBFIND algorithm at the present time.
- $M_{\rm circ,max}$: the total mass of the particles within the radius of $V_{\rm max}$.

In Fig. 2, we illustrate the ratio between the two-point correlation function of the SHAM model for the 8 parameter choices listed above and the two-point correlation function of the TNG300 hydrodynamical galaxy sample. We explore two different scenarios of applying the SHAM model: in the first scenario, we rank-order the subhalos in the DM-only simulation by some SHAM property and compute their two-point correlation function, while in the second scenario, we order the subhalos in the full-physics run and compute their two-point statistics. In both scenarios, we juxtapose these results with the auto-correlation of the full-physics subhalos rank-ordered by stellar mass. We note that typically one does not have access to the hydro simulation results, and so the results using the DM-only subhalos are of greater relevance to future mock catalog schemes. We study both scenarios in an attempt to understand the effects of baryonic physics on the quantities used in empirical models (see Section 3.2 for a more extended discussion). As is the case throughout this paper, we limit our analysis to the top 12000 subhalos in each rank-ordered list so as to avoid resolution effects and work with galaxy number densities comparable to those of current surveys such as DESI and *Euclid*.

A striking observation is that the clustering obtained using velocity-based parameters exhibits a much smaller discrepancy (with respect to the full-physics simulation) than when using the mass-based proxies for SHAM. The parameter that yields the closest match is the peak velocity, $V_{\rm peak}$, capturing the clustering on scales larger than ~ 2 Mpc/h

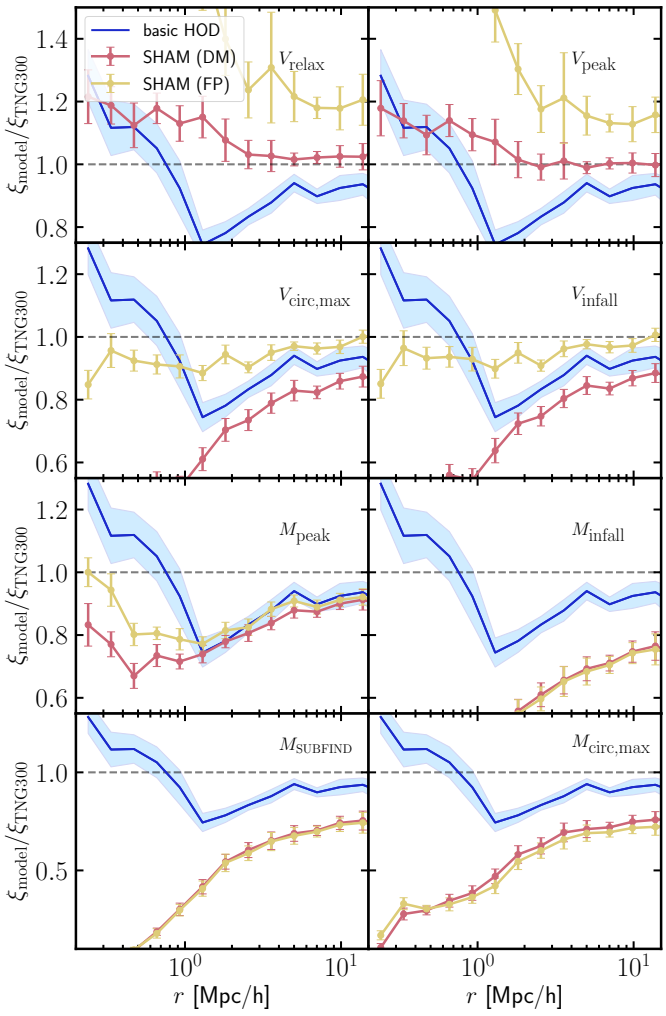

Figure 2. Ratios between the auto-correlation of the SHAM-model galaxies and the TNG300 galaxies, using different luminosity proxies for the subhalo abundance matching model (SHAM). The denominator of these ratios, i.e. the TNG300 sample, is derived by selecting the most stellar-abundant subhalos and computing their correlation function. Here we compare this with two implementations of SHAM: the first one (*red solid line*) uses the standard approach of rank-ordering the **DM-only** subhalos in terms of one of the 8 SHAM properties considered; in the second case (*gold solid line*), we have rank-ordered the **full-physics** subhalos. The DM-only curves, SHAM (DM), suggest that none of the SHAM parameters reproduces the observed clustering of the stellar-mass-selected subhalos perfectly on all scales, although $V_{\rm relax}$ and $V_{\rm peak}$ do substantially better than the rest of the parameters, particularly the mass-based ones. In the alternate SHAM model implementation, SHAM (FP), these parameters overpredict the clustering. In *shaded blue*, we show the "basic" HOD model for comparison, which exhibits a $\sim$ 12% discrepancy on large scales.

with subpercent accuracy. On scales smaller than this, however, the $V_{\rm peak}$-based SHAM model overpredicts the clustering by about 15% (see also Contreras et al. 2020). Importantly, it deviates much less than the "basic" (mass-only) HOD model when compared with TNG300. The next best performing SHAM proxy is the relaxation velocity, $V_{\rm relax}$, which overpredicts the clustering only slightly (by about 3%) on large scales. We have also experimented with introducing 0.125 dex scatter in the $V_{\rm peak} - M_{\rm star}$ relationship and have found that it results in a marginal decrease (of about $1-2\%$) in the clustering of the SHAM relative to TNG300, but it does not change the qualitative conclusions from this analysis.

Fig. 2 makes it manifestly clear that all of the mass-based SHAM proxies provide a poor fit to the galaxy auto-correlation function on all scales. The suppression in the small-scale clustering relative to TNG300 is particularly conspicuous, but even on large scales the differences are as large as 30%. The best performing mass-based parameter is $M_{\rm peak}$. However, its performance is still worse than that of the mass-only HOD sample. Interestingly, applying SHAM to the full-physics subhalos using $M_{\rm peak}$ does not boost the clustering as much as it does for the velocity-based parameters.

Comparing the *gold* and *red* curves in Fig. 2, we see that the full-physics SHAM objects are almost always more clustered than in the ordinary case where the SHAM is applied to the DM-only simulation. The only parameters for which this is not the case are the three mass parameters $M_{\rm infall}$, $M_{\rm SUBFIND}$ and $M_{\rm circ,max}$. This finding, together with the observation that for these three parameters the clustering is substantially lower than TNG300, indicates that there is no strong correlation between the abundance of luminous components and these mass-based quantities and that the inclusion of baryonic physics does not play a substantial role in improving their behavior. On the other hand, we observe a significant upsurge in the clustering for the remaining parameters. $V_{\rm relax}$ and $V_{\rm peak}$ are especially interesting, where the full-physics SHAM model yields higher auto-correlation power than TNG300. This suggests that these parameters are well-correlated with the subhalo stellar mass and are therefore good SHAM proxies. To completely reconcile the differences, one could consider introducing scatter into the relationship. The fact that the DM-only SHAM population has a lower clustering indicates that the removal of baryonic physics changes the ranking of the subhalos and likely adds stochasticity to the process. This is considered in more detail in 3.2.

As a further test, we have applied the SHAM model to only those DM-only subhalos that have matches in full physics and compared their clustering to that of the top 12000 full-physics subhalos that also have reliably found counterparts (about 91% of the 12000 most massive subhalos). This results in a marginal improvement in reconciling the clustering difference (which we do not show in Fig. 2), decreasing the inconsistencies by roughly $\sim$ 3% relative to the DM-only case. This is most likely the case since isolating only the subhalos which have survived violent disruption events mitigates some of the baryonic physics effects, but not to a sufficient degree. To fully understand the effect of small-scale galaxy processes, a more thorough investigation is needed.

3.2 Baryonic effects on the subhalos

In this section, we delve into some detail to try to understand how the inclusion of baryonic physics affects the subhalo quantities typically used in the SHAM prescription. The SHAM approach rests on the assumption that certain

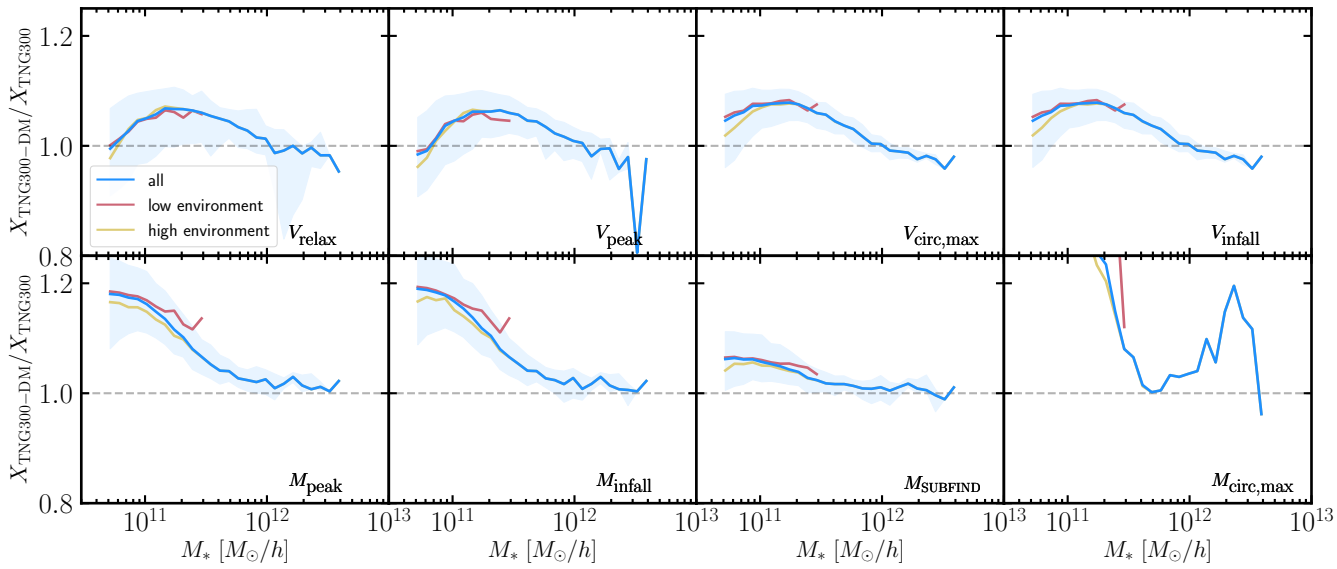

Figure 3. Ratio between the different SHAM properties in the DM-only run and their matches in the full-physics simulation: $X_{\rm TNG300-DM}/X_{\rm TNG300}$, where X denotes any one of the eight quantities used as SHAM proxies (indicated in the bottom-right of each panel), and TNG300 and TNG300-DM refer to the full-physics and dark-matter-only simulations, respectively. These show that the DM-only subhalos tend to to have consistently higher values for the various SHAM quantities when compared with their full-physics counterparts. The most substantially affected parameter is $M_{\rm circ,max}$, which provides a measure of the mass distribution in the innermost parts of the subhalo. We also show the median curves for the subhalos living in the densest (*red solid lines*) and least dense (*gold solid lines*) regions of the simulation. These imply that subhalos in dense environments tend to retain their properties when one has switched on baryonic effects.

parameters are more tightly linked to the amount of stellar material present in a subhalo and rank-ordering them is likely to recover the galaxy population more faithfully. These parameters are thought to be more resilient to well-known effects such as tidal stripping, satellite disruption and gas expulsion (in the form of AGN feedback, supernova feedback, stellar winds, etc.), meaning that these quantities are less likely to be dramatically changed by galaxy formation physics. However, Fig. 2 suggests that the SHAM quantities of interest (i.e. the ones based on velocity) do change significantly between the two simulation runs (TNG300 and TNG300-DM). We estimate the impact of these effects by tracking the same objects in the two simulations and seeing how their properties differ.

The comparison between the two simulations is illustrated in Fig. 3. The median curve and the 68-percentile contours are shown in *blue*, while in *gold* and *red*, we have selected the subhalos that live in the densest and least dense environments (divided into two equal halves), respectively. In all cases, the effects are largest $(10-20\%)$ for the smaller subhalos, which are most likely to be subjected to disk disruption events and other violent processes. We notice that the low-mass objects in the velocity-based panels display a downturn, which somewhat diminishes the differences between full-physics and DM-only. This effect is likely part of the reason that the velocity- based parameters perform overall better in our SHAM modeling (see Fig. 3). To illustrate, $V_{\rm peak}$ and $V_{\rm relax}$ are good luminosity proxies, as suggested by the *gold* curves in the two top panels of Fig. 2, and also deviate less on the low-mass end than the other 6 parameters.

In order to explain the substantial difference in the two-point correlation function between DM-only SHAM and full-physics SHAM, it is helpful to realize that the DM-only quantities have received a non-trivial amount of scatter with respect to the full-physics ones in addition to the fact that they are substantially biased (as seen in Fig. 3). Such stochasticity inevitably results in a decrease of the clustering, as this effective reordering of rank-ordered lists leads to assigning galaxies to subhalos that are in fact placed lower in the TNG300 lists. From Fig. 3, one can also notice a modest dependence of the ratio on the local environment of the subhalo. For all parameters, the low-mass DM-only subhalos living in dense environments (*gold curves*) seem slightly more similar to their full-physics counterparts.

The effect of baryons on $M_{\rm circ,max}$, which measures the mass in the inner core of the subhalo, is shown in the last panel of Fig. 3 to be particularly pronounced. The noticeable difference between the hydro simulation and the N-body simulation can be attributed to energetic feedback events which expel energy and gas outwards from the center of the subhalo. For even the larger subhalos, the full-physics cores of galaxies above 10^{12} $M_\odot/h$ are more devoid of matter. This is approximately the scale where AGN feedback becomes important in driving out gas from the inner parts of the subhalo.

Baryonic physics seems to have significant effects on our ability to match subhalos across the two simulation boxes. Out of the 12000 most massive galaxies in the full-physics simulation, we managed to find counterparts for only 91% of them. At twice this galaxy number density, the percentage of successful matches drops down by another 10%. While in some cases their particles have arbitrarily ended up in other subhalos, a substantial portion of them are in fact destroyed by galactic disks in dense environments. This could lead to

a non-negligible bias in the one-halo term, as the DM-only simulation produces more subhalos that are eligible to be populated through a SHAM algorithm while in a "true" full-physics scenario, those would have been much fewer.

We have further studied the dependence of peak and infall statistics of satellites in different environments as a function of subhalo mass. The statistics we explored in the two simulations were $\Delta M_{\rm peak|infall}$ and $z_{\rm peak|infall}$, where $\Delta M_{\rm peak|infall}$ refers to the amount of mass lost or gained when a subhalo reaches its maximum circular velocity ("peak") or when a subhalo first becomes a satellite ("infall"). No significant trends were observed apart from a larger scatter between the full-physics and DM-only redshift quantities of subhalos living in dense environments, and we hope to further analyze this in the future.

3.3 Dependence on galaxy properties

In this section, we explore how the SHAM approach performs when applied to subsamples of the galaxy populations. We consider the same population of the 12000 most massive galaxies (corresponding to a stellar mass cut of $M_{\rm star} \geq 5.1 \times 10^{10} M_\odot/h$) used in the previous section and split them into the following 5 pairs of subgroups

- **low-mass/high-mass galaxies**: we denote the subhalos with stellar masses below $8.3 \times 10^{10} M_\odot/h$ as "**low-mass**" (6000 obj.), while those above as "**high-mass**" (6000 obj.). This choice is made so that the number of objects is the same in both samples.

- **red/blue galaxies**: these are split by their $g-r$-band colors. Subhalos with $g-r > 0.78$ correspond to the "**red**" population (6000 obj.) and subhalos whose $g-r$ value is below that threshold are marked as "**blue**" (6000 obj.). The threshold is chosen so that it roughly divides in two the bimodal color-mass distribution and keeps the numbers equal. The colors are obtained by a stellar population synthesis model and convolved an SDSS filter (for details, see Nelson et al. 2018).
- **satellite/central galaxies**: we define the **"central"** (8934 obj.) to be the largest subhalo within a parent halo, while the rest of the subhalos are called "**satellites**" (3066 obj.). Note that there is only one central in every halo.
- **star-forming/quiescent galaxies**: similarly to color, the threshold here is determined as the line in sSFR-mass space (specific-star-formation-rate-mass space) that approximately separates the two modes of the galaxy population into "**star-forming**" ones (4800 obj.) and "**quiescents**" (7200 obj.), and equals $\log(\mathrm{sSFR}) = -13.86$, where the specific star formation rate is measured in units of yr^{-1}.
- **early-forming/late-forming galaxies**: these are defined by their ratio between the mass at present time (i.e., $z = 0$) and their mass at $z = 0.3$; we denote this ratio as $f_{\rm growth}$. Subhalos for which the mass gain in the past 3.5 billion years is larger than the median ($f_{\rm growth} = 0.86$) are said to be "**early-forming**" (6000 obj.), while galaxies for which the growth is smaller are "**late-forming**" (6000 obj.). The threshold is selected so that the number of objects in the two groups is roughly equal. The growth factor, $f_{\rm growth}$, can be defined self-consistently for each subhalo and thus avoids comparisons of the galaxy populations at different redshifts, which might be subject to resolution effects of the simulation or the merger tree. We have also tested other common definitions such as the redshift at which the subhalo reached half of its present mass and the redshift at which it attained its peak velocity, but none of them led to a substantial change in the qualitative interpretation.

We have also checked that regardless of how the splits are made and what number density we choose to work with, the qualitative conclusions remain unchanged.

Once we have applied the standard SHAM methodology and obtained the two lists of subhalos (12000 in each): one for the full-physics subhalos rank-ordered by their stellar masses and one for the dark-matter-only subhalos rank-ordered by $V_{\rm relax}$, we further split the full-physics galaxies into the subcategories defined above and take the dark-matter-only subhalos that have the same indices in their rank-ordered list as the indices of the full-physics objects in the selected subcategory. In this way, we investigate the question of which galaxy sub-populations are captured best after applying a simple SHAM prescription. We choose the SHAM property $V_{\rm peak}$, the highest circular velocity a subhalo attained throughout its history, since this is the best-performing SHAM parameter as seen in Fig. 2.

We compute clustering statistics via the two-point correlation function for the full-physics sub-populations and for the corresponding DM-only subset of selected subhalos. In Fig. 4, we show the ratio between the correlation functions for the 5 pairs of galaxy sub-populations listed. The first panel suggests that the clustering of the high-mass galaxies is much better-captured by the SHAM approach on small scales despite still exhibiting a discrepancy of about 20% on small scales. On the other hand, the low-mass galaxy clustering deviates significantly from the abundance-matched DM-only subhalos, differing by about 30-60% on small scales. The percentage of central galaxies in the high-mass and low-mass subgroups are 79.1% and 69.8%, respectively, which as we will see next plays a significant role in predicting the clustering.

As can be seen in the second panel, the galaxies identified as centrals tend to be more clustered by about 50% on large scales than their corresponding DM-only subhalos in the SHAM catalog. This implies that particular care should be taken when modeling the satellite population, which is discrepant by at least 50-80% on all scales. This result provides a possible explanation for why the high-mass galaxies in the first panel, which are predominantly centrals, are better modeled by SHAM. The dark-matter properties of central galaxies are perhaps more strongly correlated with their stellar masses, as assembly bias and baryonic physics affect satellites more prominently than centrals. This is because centrals live in the cores of halos and are believed to be shielded from environmental and tidal stripping effects while also being exposed to more violent merger events.

In the next two panels, we show the results for blue/red and star-forming/quiescent galaxies. The blue and star-forming sub-populations, which have a significant overlap, are substantially more clustered than their SHAM counterparts (by about $15-20\%$ on large scales and more than 50% on small scales). In contrast, the red and quiescent sub-populations underpredict the clustering, although the observed differences appear to be reconciled on large scales

to within 5 – 10%. This finding may be somewhat counter-intuitive, as we often think of the red and quiescent galaxies as being more massive and might therefore expect to see the opposite effect. However, studying the central and satellite fractions reveals that a larger percentage of the blue and star-forming galaxies are centrals (76.8% and 80.9%, respectively) than their red and quiescent counterparts (72.1% and 70.2%, respectively), which combined with the result in the second panel offers insight into why the bluer objects have stronger clustering, at least within the sample selection used here.

The final panel shows the division into early- and late-forming galaxies. It suggests a strong correlation between the large-scale distribution of the objects in a SHAM catalog obtained by conditioning on $V_{\rm peak}$ and the late-forming galaxies. One possible interpretation is that galaxies that vigorously accrete more mass relative to the remainder of the population in the last 3.5 billion years since $z = 0.3$ have had less opportunity to be stripped of their dark matter envelopes, so for them, a dark-matter property tightly coupled to their assembly history such as $V_{\rm peak}$ remains more strongly correlated with the mass of the luminous component in full-physics. Intriguingly, out of the late-forming galaxies, about 95.9% are centrals (and out of the early-forming ones 53.0% are centrals), which provides support for the above claim that the late-forming galaxies are less exposed to stripping and/or recent disruption activity.

4 HOD MODELING

In this section, we describe a framework for developing improved mock catalogs in preparation of future surveys. To alleviate the tension between the "basic" HOD model and the hydrodynamical simulation, we augment the HOD model with a secondary parameter in addition to mass. The parameters included in the extended HOD model are local environment, velocity anisotropy, virialized mass ($\sigma^2 R_{\rm halfmass}$), and total potential energy. This two-dimensional HOD model (2D-HOD) has one free parameter, r, which measures the strength of the correlation between halo occupancy and the secondary parameter within each 5% mass bin and is tuned to match the two-point galaxy correlation function of the 2D-HOD galaxies with that of TNG300. Here, we also explore alternative statistical tools to help us select the best population strategy.

To ensure that the galaxy sample from IllustrisTNG is robust, we define our galaxies as subhalos with at least 10,000 gravitationally bound star particles, which results in a galaxy sample with a number density of $n_{\rm gal} \approx 1.3 \times 10^{-3}$ $[{\rm Mpc}/h]^{-3}$. We have further checked the impact of adopting different halo finders, working with a limited simulation volume, and incorporating cosmic variance effects (for details, see Hadzhiyska et al. 2020).

4.1 Parameters

Here we review some of the parameter choices introduced in Hadzhiyska et al. (2020), which result in the most substantial shifts of the 2D-HOD galaxy auto-correlation function. In addition, we revise the definition of "local environment" in order to make it less definition-dependent. We introduce another parameter which was also found to be strongly correlated with the galaxy clustering on large scales: the total halo potential energy.

4.1.1 Velocity anisotropy

The "mass-anisotropy degeneracy" introduced by the Jeans model (Merritt 1987) predicts a strong relationship between the mass profile of a distribution of particles and the velocity anisotropy of the orbits that trace the resulting potential, Following Binney & Tremaine (1987), we define the velocity anisotropy as

$$\beta = 1 - \frac{\sigma_{\rm tan}^2}{2\sigma_{\rm rad}^2}, \tag{7}$$

where $\sigma_{\rm tan}$ and $\sigma_{\rm rad}$ are the tangential and radial velocity dispersions, respectively. We calculate these quantities over all particles in the FoF halo by projecting the velocity of each particle along and perpendicular to the radial direction (defined with respect to the position of the particle with the minimum gravitational potential energy) and then computing the standard deviation of each component (Ramakrishnan et al. 2019).

Thus defined, β depends on the shape of the halo and for that reason captures information from the full phase-space structure of the parent halo. The limits of this parameter, $-\infty$ and 1, respectively, correspond to radially and tangentially dominated velocity dispersions, while $\beta = 0$ indicates an isotropic distribution of particle orbits.

We conjecture that a plausible explanation for the relationship between a low value of β and a high galaxy clustering, found in Hadzhiyska et al. (2020), is that halos which have undergone recent accretion events tend to have particles which exhibit higher tangential velocities ($\sigma_{\rm tan}$) due to deflections caused by gravity shortly before accretion. This is particularly important for regions of high density, where mergers dominate the mass growth of halos (Fakhouri & Ma 2009, 2010), and are therefore presumed to be influential in determining the velocity structure of these halos and the richness of substructure that exists within them. As for low-density regions, accretion occurs oftentimes gradually in the radial direction since the gravitational field is dominated by the central galaxy. This results in high values of the particle velocities in the radial direction, and so the value of β increases (Fakhouri & Ma 2009; Faltenbacher & White 2010).

4.1.2 Mass measure assuming virial theorem

One of the most widely accepted choices for a virialized mass proxy is $M_{\rm 200m}$, but there are many others such as those resting on the assumptions of the virial theorem

$$\frac{GM_{\rm vir}}{R_{\rm vir}} = \sigma^2, \tag{8}$$

where σ is the dispersion velocity of the particles in the halo. Here we consider the combination $\sigma^2 R_{\rm halfmass}$, where σ is the velocity dispersion of the most massive subhalo for a given halo, while $R_{\rm halfmass}$ is the halfmass radius of the most massive subhalo.

A possible explanation for why this quantity is tied to the number of galaxies hosted by a halo is that $\sigma^2 R_{\rm halfmass}$

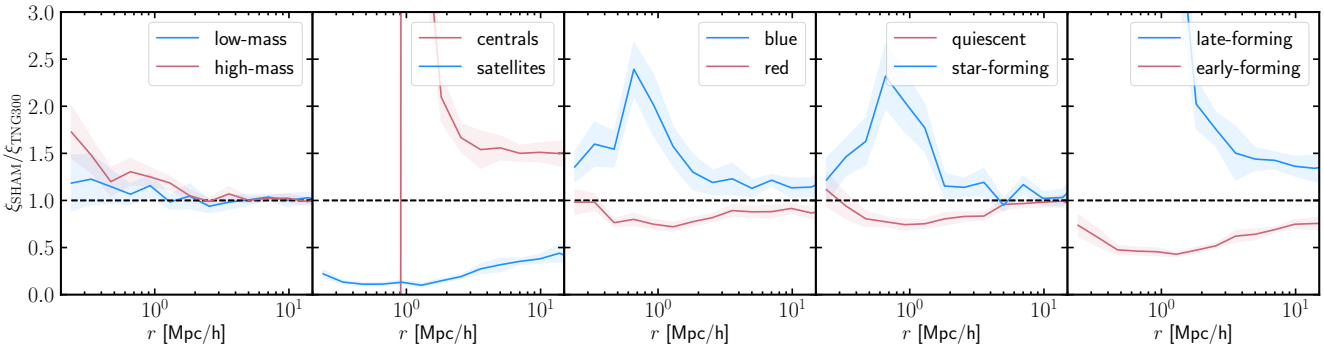

Figure 4. Correlation function ratios of SHAM-model galaxies split into different populations (defined in Section 3.3), using $V_{\rm peak}$ as the SHAM parameter. In the *leftmost panel*, we show the galaxy population split in terms of stellar mass. *First panel*: We see that the low-mass galaxies two-point function is captured better than that of the low-mass sample. *Second panel*: The clustering of the centrals is overpredicted by SHAM, while that of the satellites is significantly lower. *Third and fourth panel*: These reveal that the two-point statistics of blue and star-forming galaxies are higher than that of the rank-ordered dark-matter subhalos. *Fifth panel*: The correlation function of late-forming galaxies is significantly higher than that of their corresponding DM-only subhalos, while that of the early-forming objects is noticeably lower. The percentage of central galaxies in the late-forming sample is ~ 95.9%, which explains the visual similarity between the *fifth* and the *second* panel.

encodes a dynamical description of the halo merger history and is related to halo concentration (i.e. its central density). Its relationship with concentration is two-fold: on one hand, the dispersion velocity of the central subhalo is a dynamical proxy for the subhalo mass and the halo concentration, as more concentrated halos are expected to have relatively higher dispersion velocities of their main subhalos, and on the other, central subhalos with large $R_{\rm halfmass}$ are more likely to have consumed the smaller subhalos surrounding them resulting in higher central density. These two effects imply that there are more satellite galaxies on average for an object with a small value of $\sigma^2 R_{\rm halfmass}$.

4.1.3 Local environment

A halo residing in a dense region is expected to contain more galaxies on average than a halo in an underdense region. This is because halos in overdense regions experience more mergers, whereas those in underdense regions have more mass accreted in the form of smooth material (Abbas & Sheth 2007; Pujol et al. 2017; Paranjape et al. 2018; Shi & Sheth 2018). We assess the effects of local environment of halos on the large-scale clustering, adopting the following definition:

1. We evaluate the density field, $\delta(\mathbf{x})$, using cloud-in-cell (CIC) interpolation on a 256^3 cubic lattice of the DM particles. Each cell is of size $205/256$ Mpc$/h \approx 0.8$ Mpc$/h$.
2. We smooth the density field with a Gaussian kernel of smoothing scale $R_{\rm smooth} = 1.1$ Mpc$/h$.
3. The local environment parameter is determined by the value of the smoothed density field in the cell its center-of-potential is located in.

Conditioning on this parameter leads to a substantial increase in the galaxy clustering on large scales. In Fig. 5, we provide a visual motivation for using environment as a secondary parameter in a mass-only HOD approach. Each panel illustrates a slice of the smoothed galaxy density field split into 256^3 cells with a smoothing scale of $R = 3$ Mpc$/h$ of the "true" galaxy distribution (*left panel*), with the *right panel* painting on top the difference between the two density fields, $\Delta\delta = \delta_{\rm bHOD} - \delta_{\rm TNG300}$. Here we only present the positive values of this difference ($\Delta\delta > 0$) so as to show clearly the excess of galaxies, denoted with red circles, that the "basic" (mass-only) HOD model predicts with respect to TNG300. On the other hand, because the total occupation of the halos is preserved in the "basic" HOD model (see Section 2.3.1), the lack of red circles around the densest clusters signifies that this model fails to populate the denser clusters with enough galaxies. For this reason, considering a secondary property which preferentially populates halos living in denser environments ought to resolve some of the tension with the hydrodynamical simulation.

4.1.4 Potential energy

The gravitational potential energy of each particle is evaluated as follows

$$\Phi(\mathbf{x}_j) = -G \sum_{i=1,N}^{i\neq j} m_i g(|\mathbf{x}_i - \mathbf{x}_j|) \tag{9}$$

where $g(r)$ is the particle pair potential evaluated by AREPO. Since $\Phi(\mathbf{x}_i)$ is obtained as a summation over the entire box, it is closely related to the large-scale environmental properties around a given particle and thus serves an excellent proxy for the cosmological environment.

We explore two halo parameters derived from the particle potential energy: total potential energy and minimum potential energy. The former is defined as the sum of the gravitational potential of all particles within twice the virial radius ($= R_{\rm 200m}$) of the halo, while the latter is simply the smallest value of the potential energy across all particles within the halo. We have checked that the choice of where the summation for the total potential energy stops makes a negligible difference to the subsequent analysis. Furthermore, the results obtained by using the minimum potential energy are also very similar to those using the total potential energy. Hence, we will hereafter concentrate exclusively

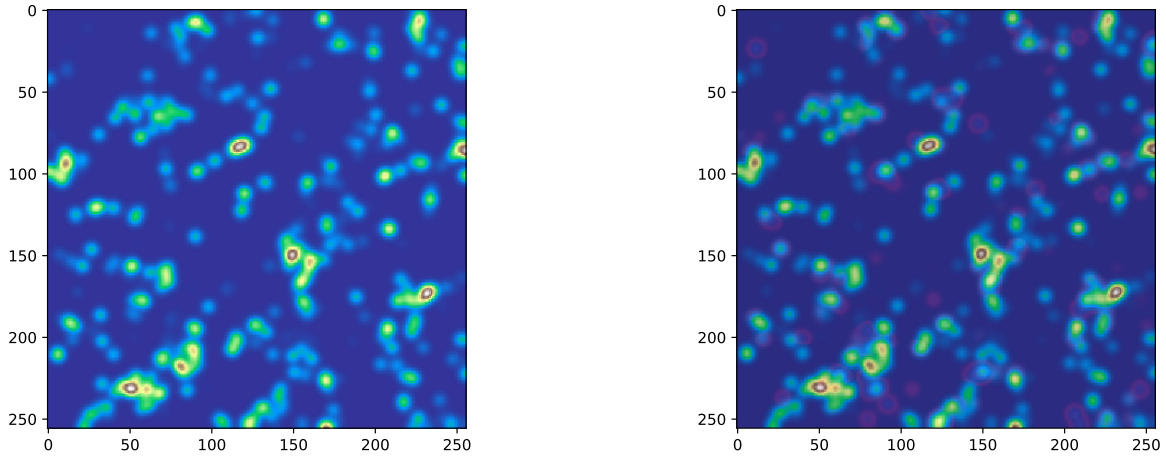

Figure 5. Visual motivation for augmenting the HOD model with an environment parameter. *Left panel:* the smoothed density field of the "true" galaxies in the TNG300 hydro simulation. *Right panel:* an overlay between the density field of the "true" galaxies (same as left panel) and the difference between that and the density field of the "basic" HOD model (in red). The red circles surrounding many of the lower-density regions indicate an excess of galaxies around smaller clusters with respect to the "true" population. These are not observed around the densest clusters, suggesting that the "basic" (mass-only) HOD model fails to supply a sufficient number of galaxies in these regions. The "basic" HOD model used here preserves the total galaxy number in the simulation, and in this figure we only show the positive difference between the two density fields, i.e. $\Delta\delta > 0$, where $\Delta\delta \equiv \delta_{\rm bHOD} - \delta_{\rm TNG300}$.

on the total potential energy parameter, but the conclusions drawn apply to our other measures of halo potential energy as well.

4.2 Statistical comparisons with the TNG300 galaxy sample

In this section, we consider alternative measures of the large-scale galaxy distribution such as cross-correlation functions, void size distributions and cumulants of the smoothed galaxy density field to compare the "fitted" 2D-HOD galaxy samples with the "true" TNG300 galaxy sample.

4.2.1 Bias and correlation coefficient

Most of the cosmological information of the matter distribution is encapsulated in the power spectrum (or correlation function) of the matter density fluctuations as a function of scale and redshift. However, galaxies are not perfect tracers of the underlying mass distribution, and thus, it is important to understand the relationship between the large-scale distribution of matter and that of galaxies. The galaxy auto-correlation function is related to the matter correlation function, $\xi_{mm}(r)$, through the real-space galaxy bias, $\tilde{b}$, in the following way

$$\xi_{gg}(r) = \tilde{b}^2(r)\xi_{mm}(r). \tag{10}$$

One of the most popular current methods for estimating the bias is through the galaxy-matter cross-correlation function, $\xi_{gm}(r)$, which can related to the matter two-point correlation function through $\tilde{b}$ and the real-space cross-correlation coefficient between matter and galaxy fluctuations, $\tilde{r}$ (Hayashi & White 2008; Desjacques et al. 2018):

$$\xi_{gm}(r) = \tilde{b}(r)\tilde{r}(r)\xi_{mm}(r) \tag{11}$$

where the galaxy bias is

$$\tilde{b}(r) = \left[\frac{\xi_{gg}(r)}{\xi_{mm}(r)}\right]^{\frac{1}{2}} \tag{12}$$

and the correlation coefficient is

$$\tilde{r}(r) = \frac{\xi_{gm}(r)}{[\xi_{gg}(r) * \xi_{mm}(r)]^{1/2}}. \tag{13}$$

In Fig. 6, we demonstrate what these look like for the baseline HOD galaxy distribution and the 2D-HOD galaxy samples compared with the TNG300 ("true") galaxy sample. We see that on large scales (larger than a few times the typical size of a dark matter halo), the galaxy bias tends to a constant value, so we can use the linear bias approximation to infer the underlying matter distribution (Peebles 1980; Mo & White 1996; Mandelbaum et al. 2013). For the linear bias approximation to be valid, the cross-correlation coefficient is also expected to be scale-independent on large scales, approaching unity (Baldauf et al. 2010). As long as one considers large-scale galaxy clustering on scales much greater than Mpc scales, the observed correlation should be sourced from the gravity field of the total matter.

In this large-scale regime, we notice that discrepancies between the galaxy auto-correlation functions of TNG300 and any galaxy population model manifest themselves in the galaxy-matter correlation function at approximately *half* their level, i.e. $\xi_{gm}(r)$ differs from the "true" galaxy population on large scales half as much as $\xi_{gg}(r)$ does because no physics besides gravity can change the large-scale bias. In addition, our simulations employ adiabatic initial conditions, so there is only one degree-of-freedom on large scales, i.e. the matter distribution.

One can explain this factor-of-2 rule in the following way. Let the "true" galaxy distribution in the TNG300 hydro simulation sample be denoted as g, and that of our al-

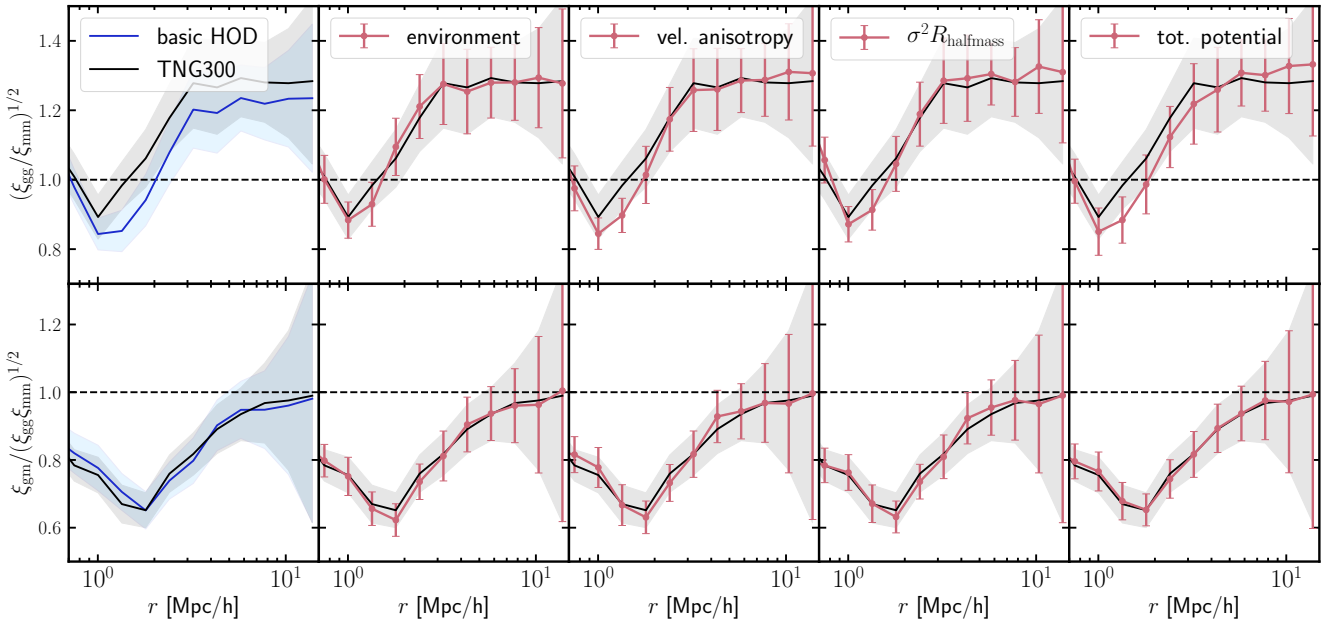

Figure 6. Bias and correlation coefficient of the "true" galaxies in TNG300 and those obtained for the HOD prescriptions considered in this paper. *Top panels*: these show the galaxy bias ($\tilde{b}(r)$) defined as the square root of the ratio of the galaxy and matter auto-correlation functions, while the *bottom panels* show the real-space correlation coefficient, $\tilde{r}(r)$. In shaded blue we show the curves for the TNG300 ("true") galaxy population, while in orange we show the "basic" (mass-only) HOD samples as well as the "fitted" 2D-HOD ones. The galaxy bias goes to a constant on large scales, and the correlation coefficient approaches 1, suggesting that a linear bias approximation on scales beyond 10 Mpc/h is appropriate. We see that the agreement between all models is excellent for the correlation coefficient, while in the case of galaxy bias, the differences are as expected from the two-point correlation statistics – namely, the "basic" HOD model has lower clustering than the "true" sample, while the 2D-HOD models show a good agreement with the hydro simulation, as they have been designed to fit it. The relatively larger size of the error bars compared with the ratio plots (shown in the rest of the paper) is due to a cancellation effect present when taking ratios of quantities.

ternative population model be $\tilde{g}$. Since on large scales, the galaxy bias can be well-approximated as linear, we can express the latter distribution as $\tilde{g} = g(1-\epsilon)$ where ϵ is a small number. The galaxy-matter power spectrum is then $\xi_{\tilde{g}m}(r) \propto (1-\epsilon)\,\xi_{gm}(r)$, while the auto-correlation function is $\xi_{\tilde{g}\tilde{g}} \propto (1-\epsilon)^2\,\xi_{gg} \approx (1-2\epsilon)\,\xi_{gg}$. So a discrepancy of $\sim 12\%$ between the auto-correlation of the "basic" HOD model and the "true" galaxy distribution (Hadzhiyska et al. 2020) is expected to manifest itself as a $\sim 1/2 \times 12\% = 6\%$ difference in the galaxy lensing probe.

However, it is important to note that while on large scales the linear bias approximation appears to be viable, it certainly breaks down on smaller scales (~ 1 Mpc/h). This has important implications for analyses using mock catalogs created via phenomenological approaches such as the HOD framework. The small-scale signal encodes a lot of information about cosmological parameters such as Ω_m and σ_8. In addition, modeling these scales correctly is a key requirement for shear analysis. Finally, the small-scale data provide an important window for probing different DM models and understanding the effects of baryonic physics. It is reassuring to see that the galaxy bias is in a reasonable agreement between the different 2D-HOD models and that the discrepancy known in the two-point correlation statistic manifests itself as expected on the galaxy bias measurement using the "basic" HOD model. The total potential 2D-HOD distribution exhibits the worst agreement with the "true" galaxy bias out of all the parameters considered – not only is it discrepant from the TNG300 galaxies, but it also shows a scale-dependence which violates the assumption of constant linear bias on large scales. Furthermore, the cross-correlation coefficients derived for all models shown in Fig. 6 exhibit a very similar behavior across all scales, suggesting that the galaxy-matter cross correlation relates similarly to the galaxy and matter clustering regardless of the underlying population model. The minimum point of the cross-correlation coefficient is on the outskirts of the halo ($r \sim 2$ Mpc/h), between the one- and two-halo terms, where the dark matter outweighs the luminous component, which has sunk to the halo center due to dynamical friction.

4.2.2 Galaxy-galaxy lensing

The cross-correlation of large-scale structure tracers with the shapes of background galaxies, referred to as stacked lensing or galaxy-galaxy lensing, offers a unique statistical method for measuring the average total matter distribution around foreground objects. Stacked lensing measurements are expected to be one of the most powerful probes for ongoing and upcoming galaxy surveys, allowing cosmologists to address fundamental physics questions such as the nature of dark energy and neutrino mass (e.g. Oguri & Takada 2011). Furthermore, by combining stacked lensing and auto-correlation measures of the same foreground galaxies, one

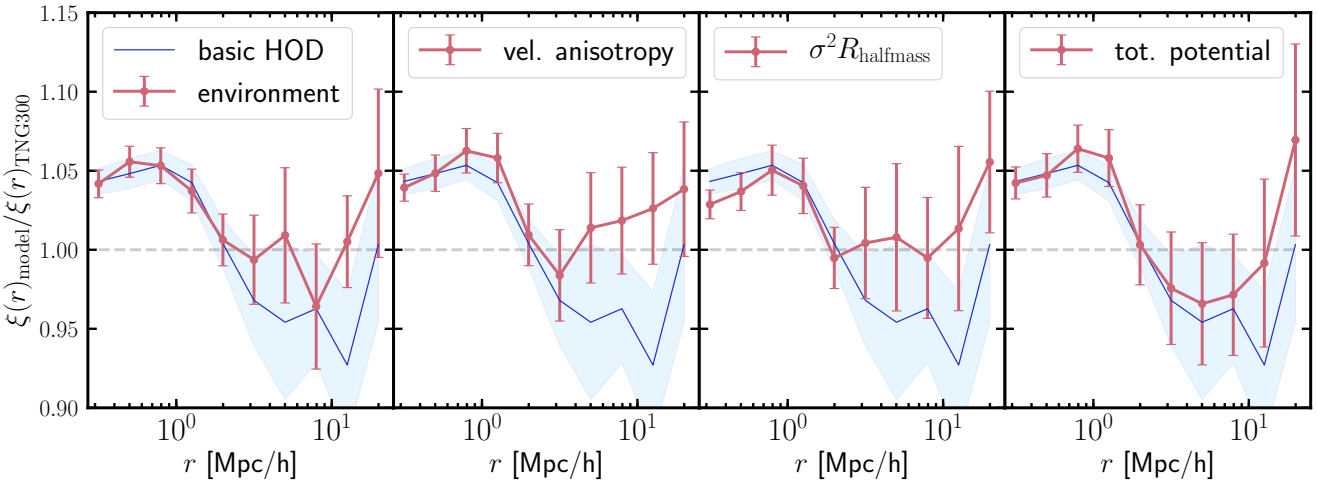

Figure 7. Ratio of the galaxy-galaxy lensing excess surface mass density between the "true" galaxies in TNG300 and those in the other HOD prescriptions considered in this paper. The shaded blue curve corresponds to the "basic" (mass-only) HOD sample, while the orange ones are obtained using the various choices of secondary parameters, tuned to match the two-point correlation function on large scales. We see that the mass-only HOD model differs noticeably on large scales by about 4%, while the "fitted" galaxy samples agree better with the TNG300 distribution. The total potential sample and the $\sigma^2 R_{\rm halfmass}$ seem to exhibit the largest amount of discrepancy.

can constrain cosmology by breaking degeneracies between galaxy bias and cosmological parameters (e.g. Seljak et al. 2005; Sunayama et al. 2020).

As a measure of the stacked lensing, here we consider the excess surface mass density profile, denoted as $\Delta\Sigma$. It is obtained by first calculating

$$\Sigma(r_p) = \bar{\rho} \int_0^{\pi_{\rm max}} \left[1 + \xi_{\rm gm}(\sqrt{r_p^2 + \pi^2})\right] {\rm d}\pi, \tag{14}$$

where $\bar{\rho}$ is the mean matter density while r_p and π are the distances perpendicular and parallel to the line of sight, respectively. Then one can find the excess surface mass density as

$$\Delta\Sigma(r_p) = \bar{\Sigma}(< r_p) - \Sigma(r_p), \tag{15}$$

where the mean surface mass density interior to the projected radius is given by

$$\bar{\Sigma}(< r_p) = \frac{1}{\pi r_p^2} \int_0^{r_p} \Sigma(r_p') 2\pi r_p' {\rm d}r_p'. \tag{16}$$

In Fig. 7, we demonstrate the excess surface mass density, $\Delta\Sigma$, for the various 2D-HOD models proposed in this work and compare them with the "basic" (mass-only) HOD in terms of their ratio with TNG300. We see that the mass-only HOD model is at a 5% tension compared with the hydro simulation on large scales, whereas the four 2D-HOD galaxy distribution proposals do a significantly better job at recovering the "true" galaxy statistic. The 5% discrepancy is approximately equal to half of the difference in the galaxy auto-correlation, validating the naive calculation outlined in Section 4.2.1. For the other four parameters, we see that all curves are in relatively good agreement with TNG300, the most prominent misfit being the total potential parameter, similarly to the conclusion drawn from Fig. 6.

These two findings together are a cause of concern for using the total potential as a secondary HOD parameter, as they suggest that this parameter fails to mimic the large-scale behavior of the galaxy clustering (i.e. the linear bias approximation) as well as its relationship with the total matter distribution at the required subpercent accuracy. The second worst 2D-HOD parameter is $\sigma^2 R_{\rm halfmass}$, which on large scales is offset from TNG300 at $> 1\sigma$. However, due to the volume limitations of TNG300, we cannot place significant importance on this observation by itself until we perform complementary tests.

4.2.3 Cumulants of the density field

Density field cumulants correspond to a set of statistics derived from measurements of the moments of the smoothed density field. They can be understood as degenerate N-point correlation functions or integrated monopole moments of the bispectrum, which are closely related to neighbor counts both in their physical interpretation as well as in their algorithmic implementation. In this work, we are interested in exploring alternative statistical tools to the two-point correlation function for quantifying and describing galaxy populations obtained from our extended 2D-HOD model. Of particular importance is the scale of galaxy clusters where we expect that galaxy population methods could exhibit substantial differences (Bernardeau 1994; Gaztanaga 1994). For this reason, we explore the regime between 3 Mpc/h and 8 Mpc/h in the subsequent analysis.

The procedure we follow can be outlined as follows:

- Divide the TNG box into 512^3 cubes of side ~ 0.4 Mpc/h and compute the counts-in-cell density field in each as $\delta_i = N_i/\bar{N} - 1$;
- Convolve it with a Gaussian filter of smoothing scale $R = \{3, 4, 5, 6, 7, 8\}$ Mpc/h to get the smoothed density field δ_R;
- Compute the second and third moments of the density contrast as $\langle\delta_R^2\rangle$ and $\langle\delta_R^3\rangle$, respectively;

• Study how the values of the two moments change as a function of smoothing scale for different galaxy distributions.

Fig. 8 illustrates plots of the second and third moment as a function of the Gaussian smoothing kernel for the TNG300 ("true") galaxies and the "basic" HOD model. One can notice that the values of the moments decrease more steeply the more smoothed the density field is, as more and more of the information on intermediate scales ($\sim$ 1 Mpc/h) gets erased. The discrepancy between the two models is even more pronounced in Fig. 9, which shows their ratio alongside the other models we test. The error bars are roughly constant across all smoothing scales (seen more clearly in Fig. 9) as in this case, the jackknifing is performed on the three-dimensional smoothed density field by consecutively excluding subboxes from it (see Section 2.4), which is independent of the smoothing scale.

In Fig. 9, we demonstrate how the second and third moments of the smoothed galaxy density field compare with TNG300 as a function of smoothing scale. Since the cumulants are closely related to the two- and three-point clustering statistics, it is not surprising (but reassuring to see) that the "basic" (mass-only) HOD model falls short of capturing the statistical behavior of the TNG300 galaxy sample. More surprising, however, is the finding that the 2D-HOD galaxy sample with $\sigma^2 R_{\rm halfmass}$ as a secondary parameter also fails that test despite being tuned to match the two-point correlation function on large-scales (more prominently observed in the third-moment panel). This indicates that conditioning on this parameter in the 2D-HOD model leads to a difference in the distribution of galaxy clusters and should make us cautious of using it for populating halos.

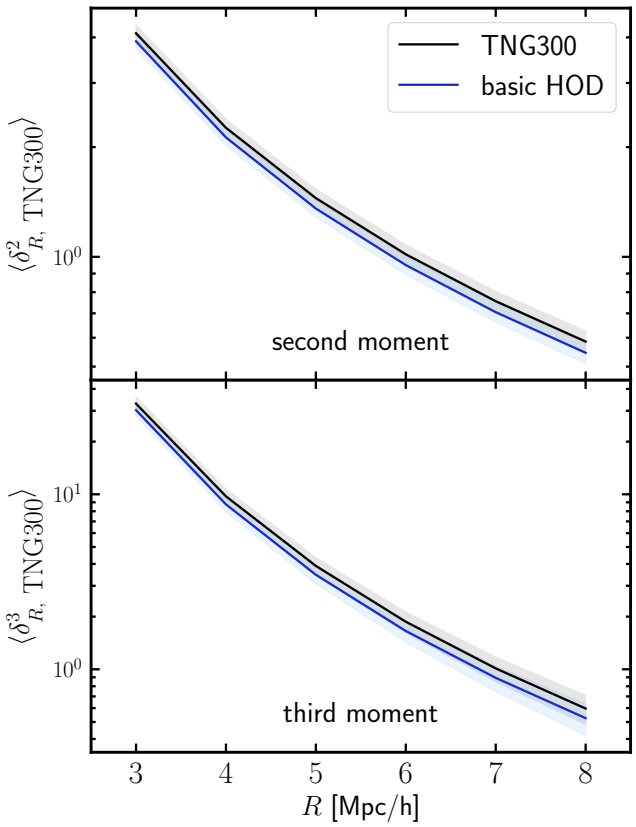

Figure 8. Second and third moment of the smoothed galaxy density field of the "true" TNG300 sample at different smoothing scales (3 – 8 Mpc/h). The errorbars are obtained by jack-knifing the final density distribution before measuring the second and third moments. As the density field gets smoother, the values of the moments rapidly decrease. The discrepancy between the two curves is illustrated more clearly in the ratio plots in Fig. 9.

4.2.4 Void statistics

Cosmic voids are large underdense regions with typical sizes of 10 – 100 Mpc/h. They have undergone very little nonlinear growth compared with halos and thus offer a pristine probe for studying cosmology (Gregory & Thompson 1978). They are sensitive to a number of effects such as redshift space distortions, baryon acoustic oscillations, neutrino signatures, and the integrated Sachs-Wolde effect (Kreisch et al. 2019, e.g.). As an example, the anisotropic galaxy distribution around voids can be used as an Alcock-Paczynski test (Alcock & Paczynski 1979). As voids are regions of low density, the average galaxy velocity in the vicinity of voids is directed outwards from the void centre. This causes a distortion of the cross-correlation of void centres and galaxy positions, as the void interior is stretched along the line-of-sight, while the void walls are squashed, e.g. Nadathur et al. (2019). Voids are complementary to both galaxy clustering and early-Universe measurements and can help break existing degeneracies between cosmological parameters.

In this work, we analyze the void size distribution and cross-correlation between galaxies and voids in real space with the intention of gaining an alternative probe of the galaxy distribution when using different population models. The number of voids as a function of their size can tell us whether the population model we employ assigns more galaxies in underdense regions than the hydro simulation, which would result in a larger number of small-sized voids at the expense of large voids. We do observe this tendency when comparing the "basic" HOD model and TNG300 but not at a significant enough level, so we do not show the result in this paper. On the other hand, if we overpopulate already dense regions, then the largest voids increase their number relative to TNG300. Neither of these effects can be confirmed with a sufficient level of precision, so we leave it for future analysis with a larger hydro simulation box. On the other hand, the location of the voids informs us where the most galaxy-deprived regions are located and cross-correlating those with the galaxy position offers insight into the relationship between large underdensities and densely clustered regions.

We have devised our own heuristic to infer the sizes and positions of the largest voids in the TNG300 box. We note that this method is not as sophisticated as some of the already existing algorithms used for void analysis, but since we are comparing the galaxy populations in a consistent way, i.e. using the same void definition, the qualitative conclusions derived are still meaningful. Our recipe is the following

• Divide the TNG box into 128^3 cubes of side $\sim$ 1.6 Mpc/h;

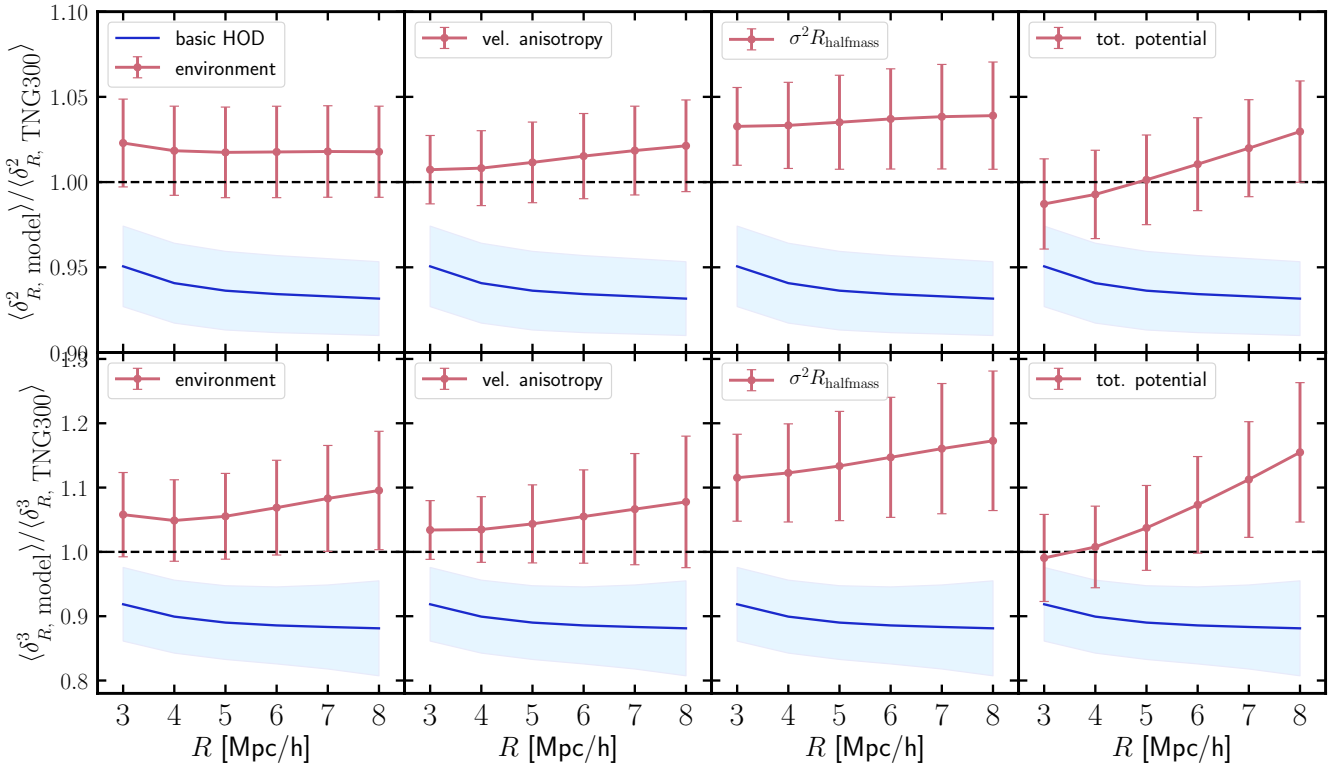

Figure 9. Ratio of the second and third moment of the smoothed galaxy density field between the 2D HOD galaxy sample and the "true" TNG300 sample (shown in Fig. 8). *The top panels* correspond to the ratios of the second moments with respect to the "true" TNG300 population, while the *bottom panels* show the ratio of their third moments. The blue shaded lines correspond to the "basic" HOD model, while orange corresponds to the "fitted" 2D-HOD models. We start smoothing at 3 Mpc/h, which is around the transition scale between the 1-halo and 2-halo terms. On larger scales, the dominant effect comes from large clusters, and we see that while the "basic" HOD model falls lower from the "truth", the other 2D-HOD models seem to exhibit a better agreement, the exception being $\sigma^2 R_{\rm halfmass}$.

- Find the distance to the *third* nearest galaxy measured from the center of each of the cubes;
- Order the thus obtained void candidates based on their size in descending order and going through each object in the list, remove all voids whose centers lie within the boundaries of that object;
- Record the void sizes and void centers for each of the population scenarios of interest.

A histogram of the void sizes for the "true" (TNG300) galaxy sample is shown in Fig. 10. The smallest voids that we find through this method are of radius of 10 Mpc/h, while the largest reach about 22 Mpc/h. These are modest sizes for voids which limit the conclusions we can draw from analyzing them. Furthermore, we work with a relatively small number of voids, on the order of 1000, so our findings are further inhibited by the void scarcity in TNG300. The overall shape of the void size distribution agrees with previous analyses (e.g. Ronconi & Marulli 2017). We do not show void size distribution comparisons with the other population models as their deviations from TNG300 are not statistically significant.

Fig. 11 illustrates the real-space cross-correlation function between voids and galaxies found in the hydro simulation (TNG300), the "basic" (mass-only) HOD model, and the four 2D-HOD models considered (augmented with one of the following secondary parameters: environment, velocity, anisotropy, $\sigma^2 R_{\rm halfmass}$, and total potential). For almost all scales considered, they are negatively correlated. There is an upsurge around $r = 8$ Mpc/h, which roughly corresponds to the smallest void size we find. On larger scales, there is a positive correlation between void centers and galaxy positions expected to keep increasing on even larger scales. The range over which we can study it, however, is limited by the simulation volume to around $r = 20$ Mpc/h. From the *bottom panel*, which shows the ratio between the cross-correlation function for the different models, we can see that the mass-only HOD model performs poorly, exhibiting a deviation of $\gtrsim 10\%$ at $r = 10$ Mpc/h. The four 2D-HOD models do substantially better, on the other hand. The largest fluctuation observed is again when using the total potential as a secondary parameter. This finding further cautions us against using this parameter in population modeling.

There is also a connection between void statistics and the moments of the density field, which stems from the fact that the high-point moments exaggerate the underdense regions and hence its average value, $\langle\xi^3\rangle$, is dominated by the underdensities. This can be seen in practice when comparing different population models in terms of the resulting void size distributions and third moments. We have done this for augmented HOD models, where we assume perfect correlation between the secondary moment (e.g. environment) and the galaxy occupation (i.e. $r = 1$, see Section 2.3.2), and

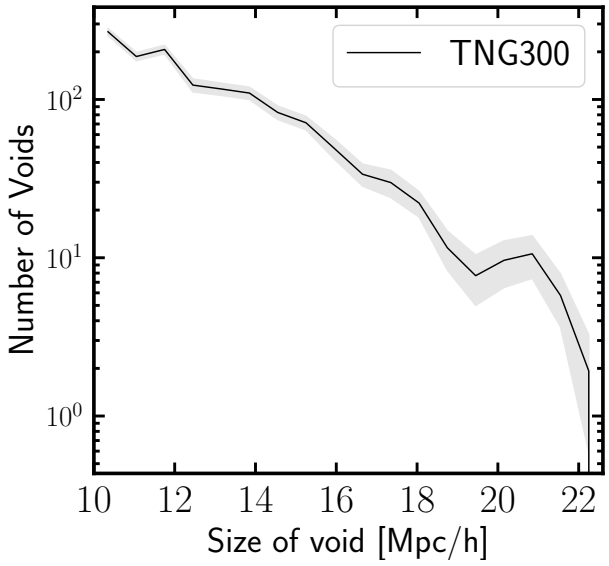

Figure 10. Number of voids as a function of their size for the "true" galaxies in TNG300. The error bars are derived from jackknifing the final void distribution. While we do not observe a strictly monotonic decrease (in log-space) for the larger voids, that is most likely the case due to their limited numbers (~ 10).

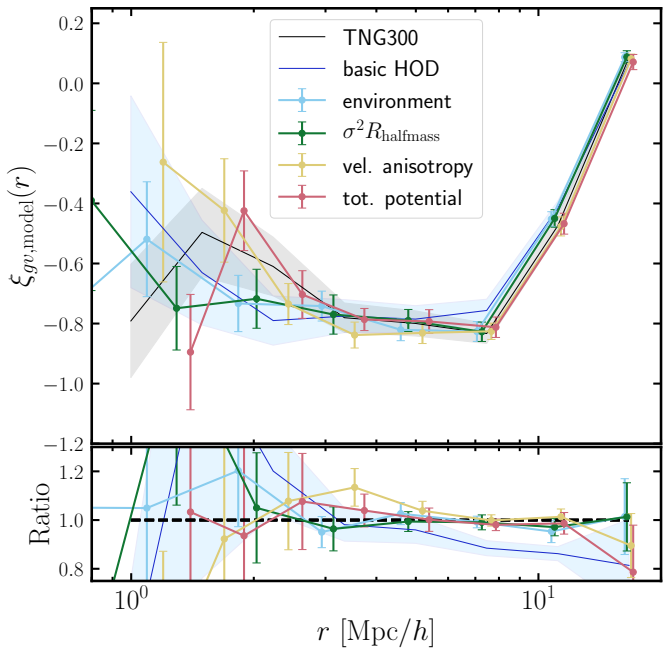

Figure 11. Galaxy-void cross-correlation function and ratio between the various HOD models presented in this work and the "true" galaxy sample. The blue shaded curves correspond to the "basic" (mass-only) HOD model, while the curves with vertical error bars to the "fitted" 2D-HOD samples. The first three 2D-HOD models (i.e. $\sigma^2 R_{\rm halfmass}$) seem to be in good agreement with the "true" population, while the basic HOD model and the total potential 2D-HOD distribution exhibits more pronounced differences especially on large scales. The voids used for this figure are of sizes 10 Mpc/h and above.

found that they have both higher third moments as well as more large voids.

5 DISCUSSION AND CONCLUSION

One of the main strengths of empirical approaches to modeling the galaxy-halo connection is that they allow us to constrain the DM distribution by using observations of the biased luminous components. Applying these models, we can obtain mock catalogs which are then used to build high-precision covariance matrices for quantifying the uncertainties in estimates of cosmological parameters. These are particularly important for next-generation large-scale structure experiments, such as DESI (Levi et al. 2013) and *Euclid* (Amendola et al. 2018). Empirical models considerably speed up the construction of mock catalogs and are widely used for forward modeling cosmological observables, e.g. Nuza et al. (2013); Leclercq et al. (2015); Kitaura et al. (2016). In addition, empirical models can complement and help improve *ab initio* models, such as hydrodynamical and semi-analytical models of galaxy formation, which tend to have more free parameters to incorporate baryon physics and are considerably more expensive to run.

In this paper, we have first explored the empirical model called subhalo abundance matching, or SHAM. We have shown that the subhalo parameters that exhibit the least amount of discrepancy compared with TNG300 are the subhalo peak velocity (i.e. the highest circular velocity it has reached throughout its history) and the relaxation velocity (the highest circular velocity it has reached throughout the times in which it satisfies a relaxation criterion defined in Section 3.1). These parameters manage to successfully reproduce the large-scale clustering to within 1% and 3%, respectively, for the number density considered ($n_{\rm gal} \approx 1.3 \times 10^{-3}$ [Mpc/h]$^{-3}$) and in particular, perform better than the "basic" HOD model. However, on small scales ($\lesssim 1$ Mpc/h), they exhibit significant discrepancies when compared with TNG300.

To understand which subcategories of galaxies are represented best by the SHAM model, we have split our sample into 5 pairs of sub-populations, based on stellar mass, color, star-formation rate, and hierarchical position in the halo (see Fig. 4). We have found that the central galaxy subpopulation seems to correlate the strongest with the large-scale distribution of the corresponding DM-only subhalos in the SHAM catalog. Introducing scatter into the $M_{\rm star} - V_{\rm peak}$ relationship would decrease the clustering and thus bring the two samples into better agreement. This result also implies that to achieve greater consistency, one ought to adopt population mechanisms which treat satellites and centrals differently. Furthermore, the high-mass, blue, and star-forming subcategories, which are predominantly made up of central galaxies in our sample, additionally boost the ratio of the clustering to their SHAM catalog equivalents. Finally, we have seen that the late-forming galaxies in our stellar-mass-cut selected sample are overwhelmingly classified as centrals ($\sim 95\%$), and therefore follow a very similar trend to that observed for the centrals.

Furthermore, we have investigated the effect of baryonic processes on subhalo properties, which may contribute sig-

nificantly to the bias between the SHAM-based and "true" galaxy distributions. It is known that energetic processes such as AGN feedback expel material from the subhalo which causes its intrinsic properties, such as its concentration, to vary considerably between the dark-matter only and the hydrodynamical simulations (Despali & Vegetti 2017; Peirani et al. 2017). We have explored how subhalos are affected across the two simulations by matching the best resolved several thousand galaxies in the full-physics run with their counterparts in the DM-only run and comparing different properties used in the SHAM model construction such as peak mass and infall velocity. This analysis reveals that the full-physics quantities are consistently lower than the dark matter ones (see Fig. 3), which suggests that tidal stripping, feedback, and galactic disk effects play a significant role in altering these parameters, which ultimately affects the relative ranking of the subhalos in full-physics and dark-matter simulations and as such leads to a decrease in the inferred clustering relative to the "true" galaxy distribution. Even at the level of the bijective matching, we have found that there is a significant fraction of the objects that have no direct matches, indicating that the inclusion of baryonic physics changes significantly the one-halo clustering term.

Another factor which influences the extracted properties of subhalos and halos from N-body simulations and thus may introduce significant systematic issues is the choice of subhalo and halo finding algorithms. Many works have recently expressed concerns about the accuracy of the most widely used Friends-of-Friends method, and alternatives such as the temporal phase-space halo finder ROCKSTAR have been viewed more favorably (Lukić et al. 2009; More et al. 2011; Knebe et al. 2011). In this paper, we have not explored the question of building population models adopting other halo finders, but leave this for the future. A full-merger tree analysis performed with ROCKSTAR opens room for interesting comparisons between the two halo finders as well as comparisons between phenomenological models such as SHAM and physically motivated ones such as semi-analytical models.

Since the large-scale clustering obtained from the IllustrisTNG 300 Mpc simulation box matches the clustering of real galaxies reasonably well (Springel et al. 2018), the extension to the HOD model developed in this paper and its subsequent statistical analysis can provide a framework for developing improved mock catalogs in preparation for future surveys. To mitigate the discrepancies observed in the large-scale clustering of galaxies, we have introduced a two-dimensional HOD (2D-HOD) model that is augmented with a secondary halo parameter in addition to mass. The parameters included in this extended HOD model are the total potential energy of the halo, its local environment, the velocity anisotropy of the particles within it, and the virialized mass measured as $\sigma^2 R_{\rm halfmass}$. There is one free parameter in this model, r, measuring the amount of correlation between halo occupancy and the secondary parameter within each 5% mass bin. We choose its value so as to reconcile the galaxy auto-correlation function on large scales ($1-20$ Mpc/h) to within $\sim 1\%$, the required precision of current cosmological efforts. We manage to do this for all 4 parameter choices listed above, the only exception being the total potential energy, where the galaxy bias is scale-dependent and does not approach constant behavior on large scales as in the other cases (see Fig. 6).

We have explored different statistical properties of the 2D-HOD galaxy catalogs and shown that despite being fitted to match only the two-point clustering of galaxies, two of our parameter choices (environment and velocity anisotropy) demonstrate an excellent agreement with TNG300 for all the examined statistical observables. We believe this to be a significant finding that merits further exploration.

We have shown that the stacked lensing of all the 2D-HOD samples is in very good agreement with TNG300, the worst choice for a secondary parameter being again the total potential energy of the halo, which might have been anticipated by our results concerning the auto-correlation function. We argue that the discrepancy observed in cross-correlation measures in real space ought to be half that found in their auto-correlation. Furthermore, our results indicate that the linear bias approximation works well on scales larger than 10 Mpc/h, where the correlation coefficient approaches 1 and the galaxy bias is roughly constant. This suggests that on these scales, baryon physics does not affect the galaxy distribution, and the dominant source that governs the galaxy distribution is gravity. We have next examined the question of whether our 2D-HOD galaxy catalogs which were constructed so as to match the two-point correlation function provide an equally good match to cross-correlation measures between the matter and galaxy distributions such as galaxy-galaxy lensing (Fig. 7) and the correlation coefficient (see Fig. 6).

The other statistical tools we have employed in this work are cosmic void statistics and cumulants of the smoothed galaxy overdensity, both of which contain higher-point information than the galaxy auto-correlation function. The analysis of the void size distribution does not yield a statistically significant difference between the different models, which is most likely due to our small-number and small-radius limitations ($\sim$ 1000 voids of maximum radius of 22 Mpc/h). Studying the void-galaxy cross- correlation function provides us with more illuminating insights that allow us to discriminate better between the different population models. In particular, the 2D-HOD model augmented with the total potential secondary parameter exhibits a larger discrepancy compared with the rest of the parameters. A caveat of our void definition is that we consider only spherically shaped voids. With a larger hydro simulation box, we could potentially begin to see more prominent differences in the different population mechanisms.

For our analysis of the cumulants of the density field, we have shown the values of the second and third moments as a function of the smoothing scale ($3-8$ Mpc/h). Of particular interest is the scale of clusters, ~ 3 Mpc/h, for which we have demonstrated that the 2D-HOD samples are roughly consistent with the "true" TNG sample, while the "basic" (mass-only) HOD model seems to deviate by more than 1σ (see Fig. 9). The worst performing secondary parameter choice is the virial mass measure $\sigma^2 R_{\rm halfmass}$. Of the 4 secondary parameters considered, across all statistics measures tried out in this paper, the best performing ones are the local environment (an extrinsic halo property) and the velocity anisotropy (an intrinsic halo property). We consider this a non-trivial result, since the 2D-HOD models have only been fitted to match the two-point clustering, and yet, two

of resulting samples exhibit a remarkable consistency with TNG300 for all statistical probes considered in this paper.

In the near future, even larger hydrodynamical galaxy formation simulations will be available, which will be extremely beneficial for expanding our knowledge of the relationship between galaxies and their dark matter halos. Once such data sets become available, we plan to test and validate the results obtained with TNG300 as well as improve the empirical population models used for creating mock catalogs. Thanks to the substantially larger number of galaxies contained in these larger volume runs, such simulations will enable us to capture the large-scale behavior even better by possibly introducing a multidimensional approach to the HOD model. Such an endeavor could potentially open the door for creating efficient galaxy population models that recover the galaxy clustering on large scales with subpercent precision and thus bridge important gaps in light of future galaxy surveys.

ACKNOWLEDGEMENTS

We would like to thank Christina Kreisch, Masahiro Takada, Charlie Conroy and David Spergel for their valuable insights and enlightening discussions. DJE is supported by U.S. Department of Energy grant DE-SC0013718 and as a Simons Foundation Investigator.

REFERENCES

Abbas U., Sheth R. K., 2007, Mon. Not. R. Astron. Soc, 378, 641
Alcock C., Paczynski B., 1979, Nature, 281, 358
Amendola L., et al., 2018, Living Reviews in Relativity, 21, 2
Angulo R. E., Baugh C. M., Lacey C. G., 2008, Mon. Not. R. Astron. Soc, 387, 921
Artale M. C., Zehavi I., Contreras S., Norberg P., 2018, Mon. Not. R. Astron. Soc, 480, 3978
Baldauf T., Smith R. E., Seljak U., Mand elbaum R., 2010, Phys. Rev. D, 81, 063531
Behroozi P. S., Conroy C., Wechsler R. H., 2010, ApJ, 717, 379
Beltz-Mohrmann G. D., Berlind A. A., Szewciw A. O., 2019, arXiv e-prints, p. arXiv:1908.11448
Berlind A. A., Weinberg D. H., 2002, Astrophys. J., 575, 587
Bernardeau F., 1994, A&A, 291, 697
Binney J., Tremaine S., 1987, Galactic dynamics
Blumenthal G. R., Faber S. M., Primack J. R., Rees M. J., 1984, Nature, 311, 517
Bose S., Eisenstein D. J., Hernquist L., Pillepich A., Nelson D., Marinacci F., Springel V., Vogelsberger M., 2019, arXiv e-prints, p. arXiv:1905.08799
Chaves-Montero J., Angulo R. E., Schaye J., Schaller M., Crain R. A., Furlong M., Theuns T., 2016, Mon. Not. R. Astron. Soc, 460, 3100
Conroy C., Wechsler R. H., Kravtsov A. V., 2006, ApJ, 647, 201
Contreras S., Angulo R., Zennaro M., 2020, arXiv e-prints, p. arXiv:2005.03672
Croton D. J., Gao L., White S. D. M., 2007, Mon. Not. R. Astron. Soc, 374, 1303
Desjacques V., Jeong D., Schmidt F., 2018, Physics Reports, 733, 1
Despali G., Vegetti S., 2017, Mon. Not. R. Astron. Soc, 469, 1997
Fakhouri O., Ma C.-P., 2009, Mon. Not. R. Astron. Soc, 394, 1825
Fakhouri O., Ma C.-P., 2010, Mon. Not. R. Astron. Soc, 401, 2245
Faltenbacher A., White S. D. M., 2010, ApJ, 708, 469
Gao L., Springel V., White S. D. M., 2005, Mon. Not. R. Astron. Soc, 363, L66
Gaztanaga E., 1994, Mon. Not. R. Astron. Soc, 268, 913
Gregory S. A., Thompson L. A., 1978, ApJ, 222, 784
Guo H., et al., 2016, Mon. Not. R. Astron. Soc, 459, 3040
Hadzhiyska B., Bose S., Eisenstein D., Hernquist L., Spergel D. N., 2020, Mon. Not. R. Astron. Soc, 493, 5506
Hayashi E., White S. D. M., 2008, Mon. Not. R. Astron. Soc, 388, 2
Hearin A. P., Zentner A. R., van den Bosch F. C., Campbell D., Tollerud E., 2016, Mon. Not. R. Astron. Soc, 460, 2552
Kitaura F.-S., et al., 2016, Mon. Not. R. Astron. Soc, 456, 4156
Knebe A., et al., 2011, Mon. Not. R. Astron. Soc, 415, 2293
Kreisch C. D., Pisani A., Carbone C., Liu J., Hawken A. J., Massara E., Spergel D. N., Wandelt B. D., 2019, Mon. Not. R. Astron. Soc, 488, 4413
Kuhlen M., Vogelsberger M., Angulo R., 2012, Physics of the Dark Universe, 1, 50
Landy S. D., Szalay A. S., 1993, ApJ, 412, 64
Leclercq F., Jasche J., Wandelt B., 2015, J. Cosmology Astropart. Phys., 2015, 015
Lee J., et al., 2020, arXiv e-prints, p. arXiv:2006.01039
Lehmann B. V., Mao Y.-Y., Becker M. R., Skillman S. W., Wechsler R. H., 2017, ApJ, 834, 37
Levi M., et al., 2013, arXiv e-prints, p. arXiv:1308.0847
Ludlow A. D., Navarro J. F., Li M., Angulo R. E., Boylan-Kolchin M., Bett P. E., 2012, Mon. Not. R. Astron. Soc, 427, 1322
Lukić Z., Reed D., Habib S., Heitmann K., 2009, ApJ, 692, 217
Mandelbaum R., Slosar A., Baldauf T., Seljak U., Hirata C. M., Nakajima R., Reyes R., Smith R. E., 2013, Mon. Not. R. Astron. Soc, 432, 1544
Mansfield P., Kravtsov A. V., 2019, arXiv e-prints, p. arXiv:1902.00030
Marinacci F., et al., 2018, Mon. Not. R. Astron. Soc, 480, 5113
McEwen J. E., Weinberg D. H., 2016, arXiv e-prints, p. arXiv:1601.02693
Merritt D., 1987, ApJ, 313, 121
Mo H. J., White S. D. M., 1996, Mon. Not. R. Astron. Soc, 282, 347
More S., Kravtsov A. V., Dalal N., Gottlöber S., 2011, ApJS, 195, 4
Nadathur S., Carter P. M., Percival W. J., Winther H. A., Bautista J. E., 2019, Phys. Rev. D, 100, 023504
Naiman J. P., et al., 2018, Mon. Not. R. Astron. Soc, 477, 1206
Nelson D., et al., 2018, Mon. Not. Roy. Astron. Soc., 475, 624
Nelson D., et al., 2019a, Computational Astrophysics and Cosmology, 6, 2
Nelson D., et al., 2019b, Mon. Not. R. Astron. Soc, 490, 3234
Nuza S. E., et al., 2013, Mon. Not. R. Astron. Soc, 432, 743
Oguri M., Takada M., 2011, Phys. Rev. D, 83, 023008
Paranjape A., Kovač K., Hartley W. G., Pahwa I., 2015, Mon. Not. R. Astron. Soc, 454, 3030
Paranjape A., Hahn O., Sheth R. K., 2018, Mon. Not. R. Astron. Soc, 476, 5442
Peacock J. A., Smith R. E., 2000, Mon. Not. R. Astron. Soc, 318, 1144
Peebles P. J. E., 1980, The large-scale structure of the universe
Peirani S., et al., 2017, Mon. Not. R. Astron. Soc, 472, 2153
Pillepich A., et al., 2018, Mon. Not. R. Astron. Soc, 475, 648
Pillepich A., et al., 2019, Mon. Not. R. Astron. Soc, 490, 3196
Planck Collaboration et al., 2016, A&A, 594, A13
Pujol A., Hoffmann K., Jiménez N., Gaztañaga E., 2017, A&A, 598, A103
Ramakrishnan S., Paranjape A., Hahn O., Sheth R. K., 2019, arXiv e-prints, p. arXiv:1903.02007
Reddick R. M., Tinker J. L., Wechsler R. H., Lu Y., 2014, ApJ, 783, 118
Ronconi T., Marulli F., 2017, A&A, 607, A24

Schaye J., et al., 2015, Mon. Not. R. Astron. Soc, 446, 521
Scoccimarro R., Sheth R. K., Hui L., Jain B., 2001, ApJ, 546, 20
Seljak U., 2000, Mon. Not. R. Astron. Soc, 318, 203
Seljak U., et al., 2005, Phys. Rev. D, 71, 043511
Shi J., Sheth R. K., 2018, Mon. Not. R. Astron. Soc, 473, 2486
Simha V., Cole S., 2013, Mon. Not. R. Astron. Soc, 436, 1142
Simha V., Weinberg D. H., Davé R., Fardal M., Katz N., Oppenheimer B. D., 2012, Mon. Not. R. Astron. Soc, 423, 3458
Springel V., 2010, Mon. Not. R. Astron. Soc, 401, 791
Springel V., White S. D. M., Tormen G., Kauffmann G., 2001, Mon. Not. Roy. Astron. Soc., 328, 726
Springel V., et al., 2018, Mon. Not. R. Astron. Soc, 475, 676
Sunayama T., et al., 2020, arXiv e-prints, p. arXiv:2002.03867
Vakili M., Hahn C., 2019, ApJ, 872, 115
Vale A., Ostriker J. P., 2007, arXiv e-prints, pp astro–ph/0701096
Vogelsberger M., et al., 2014, Mon. Not. R. Astron. Soc, 444, 1518
Vogelsberger M., Marinacci F., Torrey P., Puchwein E., 2020, Nature Reviews Physics, 2, 42
Wang K., et al., 2019, Mon. Not. R. Astron. Soc, 488, 3541
Wechsler R. H., Tinker J. L., 2018, ARA&A, 56, 435
White S. D. M., Rees M. J., 1978, Mon. Not. R. Astron. Soc, 183, 341
Xu X., Zheng Z., 2020, Mon. Not. R. Astron. Soc, 492, 2739
Yuan S., Eisenstein D. J., Garrison L. H., 2018, Mon. Not. R. Astron. Soc, 478, 2019
Zehavi I., Contreras S., Padilla N., Smith N. J., Baugh C. M., Norberg P., 2018, ApJ, 853, 84
Zentner A. R., Hearin A., van den Bosch F. C., Lange J. U., Villarreal A., 2019, Mon. Not. R. Astron. Soc, 485, 1196
Zhai Z., et al., 2019, ApJ, 874, 95
Zheng Z., et al., 2005, Astrophys. J., 633, 791

This paper has been typeset from a TEX/LATEX file prepared by the author.